

***In situ* architecture of Opa1-dependent mitochondrial cristae remodeling**

Authors

Michelle Y. Fry^{1,2,†}, Paula P. Navarro^{1,2,†}, Xingping Qin^{3,10,11}, Zintes Inde^{3,10,11}, Virly Y. Ananda¹, Camila Makhoulouta Lugo¹, Pusparanee Hakim¹, Bridget E. Luce¹, Yifan Ge^{1,2,4}, Julie L. McDonald^{1,5}, Ilzat Ali^{1,2}, Leillani L. Ha^{6,7}, Benjamin P. Kleinstiver^{6,7,8}, David C. Chan⁹, Kristopher A. Sarosiek^{3,10,11}, and Luke H. Chao^{1,2*}

Affiliations

- ¹ Department of Molecular Biology, Massachusetts General Hospital, Boston, USA
 - ² Department of Genetics, Blavatnik Institute, Harvard Medical School, Boston, USA
 - ³ John B. Little Center for Radiation Sciences, Harvard T.H. Chan School of Public Health, Boston, USA
 - ⁴ Current address: Interdisciplinary Research Center of Biology and Chemistry, Chinese Academy of Science, China.
 - ⁵ Current address: Massachusetts Institute of Technology, Biology, Cambridge, USA
 - ⁶ Center for Genomic Medicine, Massachusetts General Hospital, Boston, USA
 - ⁷ Department of Pathology, Massachusetts General Hospital, Boston, USA
 - ⁸ Department of Pathology, Harvard Medical School, Boston, USA
 - ⁹ Department of Biology, Caltech, Pasadena, USA
 - ¹⁰ Molecular and Integrative Physiological Sciences (MIPS) Program, Harvard T.H. Chan School of Public Health, Boston, USA
 - ¹¹ Lab of Systems Pharmacology, Harvard Program in Therapeutic Science, Department of Systems Biology, Harvard Medical School, Boston, MA, USA
- † These authors contributed equally, sequence was determined alphabetically. Co-first authors have agreed each reserves the right to adjust order in their CVs and public presentations of the work.

*** To whom correspondence should be addressed**

Luke H. Chao

Department of Molecular Biology, Massachusetts General Hospital, Boston, USA

Department of Genetics, Harvard Medical School, Boston, USA

e-mail: chao@molbio.mgh.harvard.edu

Keywords

Cristae remodeling, Mitochondrial biology, Apoptosis, Cryo-electron tomography, Cryo-focused ion beam milling

1 **Abstract**

2

3 Cristae membrane state plays a central role in regulating mitochondrial function and cellular metabolism.
4 The protein Optic atrophy 1 (Opa1) is an important crista remodeler that exists as two forms in the
5 mitochondrion, a membrane-anchored long form (l-Opa1) and a processed short form (s-Opa1). The
6 mechanisms for how Opa1 influences cristae shape have remained unclear due to the lack of native 3D
7 views of cristae morphology. We perform *in situ* cryo-electron tomography of cryo-focused ion beam
8 milled mouse embryonic fibroblasts with well-defined Opa1 states to understand how each form of Opa1
9 influences cristae architecture. In our tomograms, we observe elongated mitochondria with a notable
10 stacking phenotype, as well as an absence of tubular cristae, when only l-Opa1 is present. In contrast,
11 when mitochondria contain mainly s-Opa1, we observe irregular cristae packing, an increase in globular
12 cristae, and decreased matrix condensation. Notably, we find the absence of l-Opa1 results in
13 mitochondria with wider cristae junctions. BH3 profiling reveals that absence of l-Opa1 reduces
14 cytochrome c release in response to pro-apoptotic stimuli and protects cells from apoptosis induced by
15 anti-cancer agents. We discuss the implications Opa1-dependent cristae morphologies in cell death
16 initiation.

17

18

19 **Highlights**

20

- 21 • *In situ* ultrastructural characterization of mitochondrial cristae with different forms of Opa1.
- 22 • Mitochondria with predominantly l-Opa1 show cristae stacking, longer cristae compared to WT,
23 but also a reduction of globular cristae and no tubular cristae.
- 24 • Mitochondria with mostly s-Opa1 showed irregular cristae packing with wider cristae junctions
25 and more narrow cristae than WT.
- 26 • BH3 profiling show Opa1-knock-out cells have reduced apoptotic priming and reduced sensitivity
27 to apoptosis-inducing agents, and the presence l-Opa1 restores a WT protective apoptotic
28 response.

29

30 Introduction

31 Mitochondria play essential roles in energy production, metabolism and signaling, which drive the
32 biological functions and processes of the cell (**Chandel, 2014; Spinelli & Haigis, 2018; Picard &**
33 **Shirihai, 2022**). The organelle undergoes membrane remodeling during homeostatic steady-state
34 conditions through fusion and fission to generate a dynamic and responsive reticulum (**Twig *et al*, 2008;**
35 **Mishra *et al*, 2014; Mishra & Chan, 2016**). Mitochondrial ultrastructure is defined by a double-membrane
36 architecture with an outer (OMM) and inner mitochondrial membrane (IMM). The IMM can be divided into
37 three sub-regions, the cristae folds, the inner boundary membrane (IBM) and the cristae junctions (CJ),
38 which separates cristae from the IBM. Cristae in metazoans are mostly lamellar or tubular (**Hashimi,**
39 **2019**) and undergo dramatic rearrangements in response to stress and during initiation of apoptotic cell
40 death (**Frey & Mannella, 2000; Mannella, 2006; Zick *et al*, 2009**). However, we still lack mechanistic
41 understanding of how cristae are remodeled and maintain their shape.

42 Cristae are enriched with electron transport chain (ETC) proteins, making them a hub for energy
43 production (**Schägger & Pfeiffer, 2000**). These proteins directly influence cristae shape. In particular,
44 Complex V dimerization has been shown to induce positive membrane curvature to generate sharp
45 membrane bending at cristae tips and edges (**Davies *et al*, 2012; Blum *et al*, 2019**). In addition to
46 catalyzing sequential OMM and IMM merging, mitochondrial fusogens also remodel cristae. Opa1, the
47 IMM fusogen, has been functionally implicated in CJ maintenance and cristae remodeling during
48 apoptosis. The initial steps of apoptosis involve cytochrome c release from the cristae lumen, where
49 ~85% of the cellular cytochrome c is stored. Expression of wild-type (WT) Opa1 has been reported to
50 protect against apoptosis by restricting cytochrome c release, whereas the loss of Opa1 has been
51 reported to result in mitochondria fragmentation and enhanced cytochrome c release (**Scorrano *et al*,**
52 **2002**). There is also functional evidence for a link between Opa1 processing and protection against
53 apoptosis initiation (**Cipolat *et al*, 2006**). Opa1 is processed by inner-membrane proteases, such as
54 Oma1, Yme1L, and Parl, to generate a 'soluble' form that lacks the N-terminal transmembrane (TM)
55 segment (s-Opa1) (**Song *et al*, 2007; Anand *et al*, 2014**). This results in two forms of Opa1 in the
56 mitochondria: s-Opa1 and the unprocessed, full N-terminal TM anchored long form (l-Opa1).

57 Previous work used transmission electron microscopy (TEM) imaging of chemically fixed and
58 heavy metal-stained cells to investigate the role of Opa1 in cristae shape. Knock-downing Opa1 induced
59 more disorganized, globular and hyper-convex cristae, whereas over expression of Opa1 resulted in
60 narrower cristae and CJs (**Frezza *et al*, 2006**). In contrast, the addition of pro-apoptotic peptides resulted
61 in wider CJs. These observations suggest the organelle's inner-membrane functional state may be highly
62 sensitive to the levels and forms of Opa1 present, and the membrane architectures supported by Opa1.
63 We previously showed that stoichiometric levels of both l- and s-Opa1 are required for fast and efficient

64 membrane fusion *in vitro* (**Ge et al, 2020**); however, *in situ* structural understanding of how cristae shape
65 is maintained by Opa1 has been lacking.

66 To understand the role of Opa1 forms in cristae morphology maintenance and remodeling *in situ*,
67 we investigated the state of mitochondrial membranes in mouse embryonic fibroblasts (MEFs) with
68 different levels of s- and l-Opa1 by applying *in situ* cryo-electron tomography (cryo-ET) of cryo-focused
69 ion beam (cryo-FIB) milled cells. We used defined cell lines that predominantly contained either l-Opa1
70 or s-Opa1 to understand how mitochondrial membrane architecture and shape depend on the expression
71 levels and form of Opa1. Here, we present an extensive characterization of the morphological properties
72 of mitochondrial cristae membranes. We observe that l-Opa1 contributes to cristae stacking, longer
73 cristae, a reduction of globular cristae and the maintenance of inter-membrane space (IMS) volume and
74 cristae junction width. We find that the presence of s-Opa1 correlates with tubular cristae, wider cristae
75 junctions, more narrow cristae, and irregular cristae packing. Using BH3-profiling, we compared apoptotic
76 responses in these cell lines and observed WT-like responses only in the cells with l-Opa1 present, while
77 cells with predominantly s-Opa1 and Opa1 knock-out cells were resistant to apoptosis. Our work
78 demonstrates that both forms of Opa1 play distinct roles in maintaining membrane distances and shapes
79 important in mitochondrial cristae architecture, revealing specific roles of s- and l-Opa1 beyond
80 mitochondrial fusion.

81

82 Results

83

84 *In situ* morphology of mitochondria with different Opa1 processing.

85 To understand mitochondrial ultrastructure regulation by Opa1, we probed cell lines that differed
86 in the expression level and processed state of Opa1 (**Fig. S1**). In this study, we utilized five MEFs cell
87 lines: (i) wild-type (WT) cells, (ii) Opa1 overexpressing cells (Opa1-OE), (iii) a Δ exon5b CRISPR MEF
88 line with an Opa1^{-/-} background, which restricts Opa1 cleavage and results in the presence of mostly the
89 long-Opa1 (l-Opa1) isoform (referred to as l-Opa1* in this work), (iv) an Opa1 knock-out (Opa1-KO) line
90 expressing the Opa1 isoform 5, which is robustly processed and results in the presence of the short-
91 Opa1 (s-Opa1) isoform (referred to as s-Opa1*) and (v) Opa1-KO (**Mishra et al, 2014; Wang et al, 2021**)
92 (**Fig. S1**).

93 MEFs lamellae ~200-350 nm thick were generated by cryo-focused ion beam (cryo-FIB) milling
94 for subsequent *in situ* cryo-electron tomography (cryo-ET) imaging (**Rigort et al, 2012; Mahamid et al,**
95 **2016**), following a previously established imaging pipeline (**Navarro et al, 2022**). A total of 100 tilt-series
96 (WT = 33, Opa1-OE = 7, l-Opa1* = 27, s-Opa1* = 22 and Opa1-KO = 11) were acquired, aligned and
97 three-dimensionally (3D) reconstructed into tomograms (**Table S1**). To improve mitochondrial membrane
98 visualization, we denoised our cryo-electron tomograms using Topaz-Denoise (**Beppler et al, 2020**). Note
99 that cryo-electron tomograms only covered a section of the mitochondria contained within the thickness
100 of the lamella, thus, all mitochondria were partially imaged in the Z-axis. In some cases, due to the trade-
101 off between resolution and field of view (**Navarro, 2022**), mitochondria are only partially visible in the XY
102 plane (**Fig S2a**). Densities corresponding to the inner mitochondrial membrane (IMM) and the outer
103 mitochondrial membrane (OMM) were 3D segmented in yellow and green, respectively (**Fig.1a, Movies**
104 **1-5**).

105 Mitochondria were classified into ellipsoidal, round, partial (when partially imaged in the XY plane)
106 or polygon categories based on visual morphological analysis. Most mitochondria are ellipsoidal in all cell
107 lines except for s-Opa1* where round mitochondria dominate (**Fig. 1b**), which correlates with smaller
108 mitochondrial area (**Fig. 1c**). Mitochondria in WT cells are larger in area ($0.34 \pm 0.03 \mu\text{m}^2$) than in other
109 conditions; with, on average, smaller mitochondria in l-Opa1* cells ($0.2 \pm 0.02 \mu\text{m}^2$) and significantly
110 smaller mitochondria in Opa1-OE ($0.14 \pm 0.02 \mu\text{m}^2$) and s-Opa1* cells ($0.18 \pm 0.02 \mu\text{m}^2$) (**Fig. 1c**).

111 Since the sample size of our cryo-ET is limited, and acquisition areas were determined based on
112 regions of high mitochondrial abundance, we characterized all cell lines by live-cell fluorescence
113 microscopy (FM) and conventional transmission electron microscopy (TEM). Consistently, we found by
114 live-cell FM that WT and l-Opa1* lines have elongated mitochondrial networks, while the Opa1-KO and
115 s-Opa1* lines have fragmented networks, suggesting healthy fusion activity in WT and l-Opa1* cells, and

116 corroborates the results from the cryo-ET data (**Fig. S3, Movie 6**). Furthermore, conventional TEM
117 imaging of the cell lines also shows that most mitochondria are ellipsoidal, aligning well with the cryo-ET
118 data (**Fig. S4a, b**). Mitochondrial matrix density was classified as normal, dark, uneven or empty, which
119 reflects brighter matrix staining (**Fig. S4c**). Matrix staining is prone to artifacts introduced by
120 heterogenous heavy-metal stain and/or resin embedding. In the TEM data, mitochondria in Opa1-OE
121 cells are larger and less abundant but cover more area per cell than WT. Aligned with previous reports
122 (**Gómez-Valadés et al, 2021**), mitochondria from Opa1-KO cells are larger than WT, but have a similar
123 abundance and total mitochondrial area per cell as WT (**Fig. S4d**). Interestingly, both mitochondria in I-
124 Opa1* and s-Opa1* cell lines display fewer mitochondria per cell, with less total mitochondrial area per
125 cell than WT, despite differences in mitochondrial size (**Fig. S4e-f**).

126 By cryo-ET, we observed an overall higher percentage of mitochondria displaying a stacking
127 cristae phenotype in mutant cell lines, as compared to WT. This phenotype, defined as mitochondria
128 presenting three or more lamellar cristae running in parallel to one another across the mitochondrial
129 matrix throughout the tomogram (**Fig. S5a**), was observed in 23.53% of the mitochondria from WT cells.
130 In Opa1-OE and I-Opa1* cells, 52.94% and 53.85% of the mitochondria show stacking cristae,
131 respectively (**Fig. S5b**).

132 In addition, we also found significantly greater cristae density (cristae/ μm^2) in mitochondria from
133 Opa1-OE, I-Opa1*, and s-Opa1* cell lines relative to WT cells (**Fig. S2b**), indicating that alterations in
134 Opa1 levels or form can impact the steady-state number of cristae in a given mitochondrial volume.
135 However, the number of cristae per mitochondria does not significantly vary across cell lines (**Fig. S2c**),
136 which can be explained by an overall reduced size for mitochondria in these lines. Furthermore, greater
137 variation in cristae density is observed in s-Opa1* mitochondria compared to the other cell lines. In I-
138 Opa1* cells, we observed organized and parallel oriented cristae mitochondria, whereas cristae from s-
139 Opa1* cells do not exhibit such a pattern or organization and frequently cross over one another (**Fig. 1a,**
140 **S2a and S5a**).

141

142 ***In situ* cristae ultrastructure**

143 We next characterized the architecture of cristae and the morphological dependence on the
144 expression level and form of Opa1 present by *in situ* cryo-ET. Previous work focused on membrane
145 changes related to cytochrome c mobilization during apoptosis (**Scorrano et al, 2002; Frezza et al,**
146 **2006**). As cytochrome c is predominantly stored within the crista lumen, changes in the cristae
147 architecture were suggested to facilitate release of luminal contents, specifically widening of crista and
148 CJ, as observed by fixed-stained TEM. However, questions related to the specific roles for I-Opa1 and s-
149 Opa1 in the cristae membrane states were inaccessible.

150 We formally analyzed the direction of cristae relative to the OMM across cell lines and quantified
151 cristae connectivity, categorizing cristae as straight, tilted, or disconnected (with no observed attachment
152 to the inner boundary membrane (IBM)). A larger percentage of cristae in I-Opa1* and Opa1-KO cells fall
153 into the disconnected category compared to WT (**Fig. 2a**). Cristae were classified based on shape into
154 canonical lamellar, globular and tubular categories (**Harner et al, 2016**). Cristae that did not fall into these
155 categories were classified as unusual. In all cell lines, most observed cristae are lamellar (**Fig. 2b**), but
156 mitochondria in Opa1-OE cells present higher proportion of unusual cristae. Interestingly, the proportion
157 of lamellar cristae increases in the mutant Opa1 cell lines, with I-Opa1* and s-Opa1* cells exhibiting 81%
158 and 77% lamellar cristae, respectively. This suggests that altered levels of Opa1 affect the steady-state
159 proportion of lamellar cristae. Indeed, cells with altered levels and forms of Opa1 (Opa1-OE, I-Opa1* and
160 s-Opa1* lines) have a reduced proportion of tubular and globular cristae, with a greater variation of cristae
161 shape observed in s-Opa1* cells (**Fig. 2b**). Tubular cristae are absent in I-Opa1* and Opa1-KO cells,
162 suggesting that the presence of s-Opa1 sustains a tubular cristae morphology. However, the I-Opa1* and
163 Opa1-KO lines differed in their percentages of globular cristae observed: 1.7% and 13.5%, respectively.
164 For the other cell lines, the percentage of globular cristae is 5.5% for WT, 2% for Opa1-OE and 3.5% for
165 s-Opa1* cristae, indicating that overexpression of both forms of Opa1 (Opa1-OE), or presence of only
166 one form of Opa1 (I-Opa1*, s-Opa1*), results in a reduced proportion of globular cristae (**Fig. 2b, S2a**).

167 We sought to determine how cristae length and width are affected by each form of Opa1 by
168 measuring the 3D length and width of fifty cristae per cell line in our tomograms (**Fig. S6a, b**). Previous
169 fixed-stained studies found Opa1 over-expression resulted in increased cristae length. We observed by
170 cryo-ET, I-Opa1* and Opa1-KO mitochondria have significantly longer cristae than WT, and s-Opa1*
171 mitochondria also possess longer cristae than WT (**Fig. 2c**). In terms of width, cristae in s-Opa1* cells
172 are significantly narrower than in WT cells, while cristae in Opa1-KO cells are significantly wider,
173 correlating with the percentage of globular cristae present in each of these cell lines (**Fig. 2b, d**). However,
174 there are notable differences when analyzing the distribution of cristae width values across cell lines (**Fig.**
175 **2e**). Mitochondria in Opa1-OE and I-Opa1* cells have the same average cristae width as WT
176 mitochondria; however, both present a wider distribution of cristae widths, with many values falling into
177 0-5 nm and 9-14 nm-width ranges. In contrast, mitochondria in WT cells show only one narrow peak
178 between 9-16 nm (**Fig. 2e-f**). This suggests that cristae in Opa1-OE and I-Opa1* cells also include a
179 significant proportion of cristae with other widths. Upon closer inspection, we found many of these cristae
180 show zipped or pinched morphologies (**Fig. 2e**). Mitochondria in s-Opa1* cells show an average width
181 ranging from 6-15 nm, which is significantly smaller than WT; though the majority of values fell within this
182 peak similar to WT (**Fig. 2d, f**). In Opa1-KO mitochondria, the width distribution peak ranges from 10-17

183 nm, with an outlier representing a population of extremely wide cristae also seen in I-Opa1* mitochondria.
184 This outlier represents a class of globular cristae (**Fig. 2b, d-f**).

185 Cristae that did not fall into the lamellar, globular, or tubular categories were classified as unusual.
186 We defined eight unusual shapes: (i) loop, where cristae curve and connect to IBM via two CJs; (ii) split,
187 where cristae branched into two or more cristae; (iii) straight-across, when cristae are perpendicular and
188 connect to the IBM via two CJs; (iv) amorphous, when cristae display a nebulous morphology; (v) ring,
189 where cristae are circular; (vi) pinched, where cristae show areas where membranes touch; (vii) zipped,
190 when cristae have regions where both membranes merge until both cannot be distinguished; and (viii)
191 vesicular, where material is observed within the cristae (**Fig. S7**). Of these categories only four unusual
192 shapes were observed in WT MEF mitochondria - ring, loop, straight-across, and split; the loop phenotype
193 was dominant (**Fig. S7a**). These shapes were also observed in Opa1-OE mitochondria, as well as a
194 notable number of pinched and zipped cristae. In contrast, very few cristae in Opa1-OE mitochondria
195 form loops and instead most fall in the zipped and pinched categories. Interestingly, no zipped cristae
196 were observed in WT or Opa1-KO cells and only one zipped crista was observed in s-Opa1* cells,
197 suggesting that the membrane anchored I-Opa1 may play a role in bridging the two membranes of the
198 cristae for long stretches. Numerous cristae rings were observed in Opa1-OE, s-Opa1* and Opa1-KO
199 mitochondria, but not in WT and I-Opa1* and mitochondria. Only one crista from WT cells fell into the ring
200 category. Nearly a quarter of the observed cristae from I-Opa1* mitochondria are amorphous and one
201 fifth of the cristae in these mitochondria are straight-across, connecting to the IMM at two different
202 locations. No amorphous cristae were observed in Opa1-OE cells and no straight-across cristae were
203 observed in Opa1-KO cells. Pinched cristae were not observed in the WT MEF cell lines, with over 30%
204 of cristae from both Opa1-OE and Opa1-KO mitochondria classified as pinched (**Fig. S7a**).

205

206 **Cristae junction morphology by cryo-ET**

207 We measured and analyzed CJs from summed projected central slices of tomograms for all cell
208 lines. CJs were defined as the site where the crista membrane joins the boundary region of the IMM (**Fig**
209 **S6c**). Consistent with previous reports, we observed widening of CJs in Opa1-KO mitochondria, relative
210 to WT (**Fig. 3a**). Intriguingly, we found that CJs are also significantly wider in s-Opa1* (**Fig. 3a**). We did
211 not find any significant difference in CJ width between I-Opa1* and Opa1-OE mitochondria.

212 As we noted in our initial inspection of tomograms, a greater proportion of cristae in s-Opa1*
213 mitochondria are tilted, where the crista length was not arranged relative to the IBM at a 90-degree angle
214 (**Fig. 2a**). To further investigate if this tilt occurs at the start of the cristae or if the cristae kink, we quantified
215 the angle at the CJ (**Fig. S6d**). While most cristae are orthogonal to the OMM, we observed a wide range
216 of CJ angles in s-Opa1* mitochondria. Overall, the CJ angles in s-Opa1* cristae are less perpendicular

217 compared to WT CJs, consistent with our observation of more tilted cristae in these cells (**Fig. 2a and**
218 **3b, c**).

219 We also found that some cristae have two or more CJs. The majority of mitochondria from I-Opa1*
220 mitochondria (77%) have at least one crista with multiple junctions, which is considerably higher than WT
221 (35%), Opa1-OE (30%), s-Opa1* (27%), and Opa1-KO (25%) (**Fig. S7a**). These multijunction cristae
222 were classified as straight-across or loop, correlating with the high percentages of these phenotypes
223 found in I-Opa1* (**Fig. 3b and S7**). In WT cells, there is an equivalent number of straight-across and loop
224 cristae with more than one CJ. In Opa1-OE and I-Opa1* mitochondria the majority of multijunction cristae
225 fell into the straight-across category, whereas in s-Opa1* and Opa1-KO mitochondria, the majority of
226 multijunction cristae were of the loop class (**Fig. S8b**).

227

228 ***In situ* characterization of mitochondrial subcompartments**

229 We analyzed the volume occupied by the mitochondrial subcompartments: matrix, inner
230 membrane space (IMS) and cristae lumen (CL) in our cryo-electron tomograms (**Fig. 4a**). We 3D-
231 segmented 5 mitochondria per cell line, and measured the volumes occupied by the entire mitochondria
232 and each subcompartments, comparing changes in 3D volume (**Fig. 4b-f**). Relative to WT, the overall
233 mitochondrial volume in all other cell lines is reduced, with s-Opa1* mitochondrial volume significantly
234 smaller (**Fig 4b**). IMS volume appears similar in all cell lines except for s-Opa1* and Opa1-OE
235 mitochondria, which both show larger relative IMS volume (**Fig. 4c**). The CL occupies the lowest relative
236 volume in WT, occupying significantly higher relative volumes in I-Opa1*, s-Opa1* and Opa1-KO
237 mitochondria (**Fig. 4d**). Consistently, the relative matrix volume is smaller in these cell lines compared to
238 WT (**Fig. 4e, f**). While the average matrix volumes are similar for I-Opa1* (76.99%) and s-Opa1* (78.63%),
239 in s-Opa1* cells a greater fraction of the overall volume comprises of the IMS (**Fig. 4c, e, f**). Taken
240 together, the absence of I-Opa1 results in larger IMS volumes, suggesting that I-Opa1 may play a role in
241 maintaining WT OMM-IMM distances. We also observed significantly increased CL volumes in I-Opa1*
242 and s-Opa1* mitochondria relative to WT and noted a slightly reduced CL volume in s-Opa1* cells
243 compared to I-Opa1* cells. This difference in CL volume indicates that an imbalance of I- and s-Opa1
244 levels result in larger CL volumes.

245 We observed distinct differences in matrix texture by cryo-ET when quantifying the grey scale
246 levels in normalized summed projected images from cryo-electron tomograms (**Fig. 4g**). The
247 mitochondrial matrix is denser in Opa1-OE, I-Opa1* and Opa1-KO compared to WT, while the matrix in
248 s-Opa1* cells is less dense, as reported by a brighter grey scale value (**Fig. 4g**). Notably, the darker
249 mitochondrial matrix in the Opa1-OE cell line can be attributed to the presence of electron dense deposits
250 within the mitochondrial matrix, likely to be calcium phosphate (**Wolf et al, 2017; Strubbe-Rivera et al,**

251 **2021) (Fig. 1a and S2a white arrowheads)**. These observations indicate that absolute and relative
252 levels of Opa1 forms not only affect mitochondrial morphology and cristae architecture, but also influence
253 matrix content.

254

255 **BH3 profiling data**

256 To uncover any potential effects of Opa1 perturbations on the apoptosis pathway, we used BH3
257 profiling to compare mitochondrial responses to pro-apoptotic stimuli across the cell lines. BH3 profiling
258 quantifies the percentage of cells that release cytochrome c from their mitochondria, the key commitment
259 step in mitochondrial apoptosis, in response to treatment with BH3 peptides that mimic the activity of pro-
260 apoptotic proteins from the BCL-2 family (**Fraser et al, 2018**). Cells that release cytochrome c in response
261 to moderate or weak pro-apoptotic stimuli are considered to be primed for apoptosis, whereas cells that
262 require strong stimuli to trigger cytochrome c release are unprimed. Apoptotic priming has been
263 previously shown to determine whether healthy and cancerous cells undergo apoptosis in response to
264 cellular stress or damage (**Chonghaile et al, 2011; Sarosiek et al, 2017; Spetz et al, 2022**). In the MEF
265 lines tested, BH3 profiling showed a substantial reduction in apoptotic priming of Opa1-KO MEFs relative
266 to WT controls as indicated by decreased sensitivity to the BIM BH3 peptide, which can inhibit all pro-
267 survival BCL-2 family proteins and also directly activate BAX and BAK (**Fig. 5a**). We also used a
268 chemosensitivity assay to measure apoptotic sensitivity by quantifying markers of apoptosis (in this case,
269 Annexin V positivity) after treatment of cultured cells with common apoptosis-inducing drugs. Equal doses
270 of the BIM BH3 peptide induced less cytochrome c release from mitochondria in Opa1-KO MEFs than
271 WT MEFs, indicated that stronger pro-death stimuli are required to induce apoptosis in cells lacking Opa1
272 (**Fig. 5a**). We also tested MEF sensitivity to common apoptosis-inducing agents by quantifying Annexin
273 V, a marker of early apoptosis, after treatment. Based on the BH3 profiling results, we would expect less
274 apoptosis after treatment of Opa1-KO MEFs than WT MEFs. We found that indeed this was the case:
275 Opa1 KO MEFs were more resistant to treatment with the topoisomerase inhibitor etoposide, DNA
276 damaging agent doxorubicin, and pan-kinase inhibitor staurosporine at 24 hours (**Fig. 5c**). Similar
277 differences in sensitivity were also detected at 48 and 72 hours, suggesting that retention of cytochrome
278 c durably protected Opa1 KO cells from commitment to apoptosis (**Fig S9a,b**).

279 In the BH3 profiling data, the s-Opa1* MEFs show levels of apoptotic priming between WT and
280 Opa1-KO MEFs, while the l-Opa1* MEFs behave similarly to the WT MEFs in most conditions (**Fig. 5a**).
281 These results suggested that these lines would not be as resistant to apoptosis-inducing agents as the
282 KO cells. This was evident in the 24 hour chemosensitivity data for etoposide, doxorubicin, and
283 staurosporine treatment (**Fig. 5c**) as well as data at 48 and 72 hours post-treatment (**Fig. S9a,b**). Finally,

284 we investigated the apoptotic sensitivity of Opa1-OE cells, and found that in general these cells showed
285 similar behavior to WT cells (**Fig. 5b,c, S9a,b**).

286

287 Discussion

288 Understanding how sophisticated membrane architectures are generated in pleiomorphic
289 organelles poses a challenge and an opportunity for structural cell biology. The mitochondrion is an
290 exemplar case where the organelle's morphology can take on a wide range of forms. This plasticity is
291 particularly challenging to understand when multiple protein complexes cooperatively regulate such
292 morphologies, and these proteins vary in abundance, while occupying multiple conformational states and
293 species.

294 Here, we focused on how Opa1 regulates mitochondrial ultrastructure, in particular cristae
295 morphology. The majority of previous analyses of mitochondrial cristae morphology have come from
296 conventional TEM micrographs of fixed and heavy metal-stained cells (**Scorrano et al, 2002; Olichon**
297 **et al, 2003; Frezza et al, 2006**). Using state-of-the-art *in situ* cryo-ET, we analyzed mitochondria in cell
298 lines where the Opa1 state was well defined. We found notable new morphological differences specific
299 to the form of Opa1 present (**Fig. 6**). We observe that when only s-Opa1 is present, cristae junctions are
300 wider than WT CJs, there is a less condensed matrix, and an increased IMS volume. We also find more
301 stacked cristae, more multi-junction cristae, and lack of tubular cristae when only l-Opa1 is present.

302 Previous TEM imaging showed that cytochrome c release (stimulated by pro-apoptotic signaling
303 proteins such as BID), results in rearrangement of mitochondrial ultrastructure such as the opening of
304 cristae junctions and widening of the cristae lumen, which are counteracted by Opa1 over-expression
305 that results in tightening cristae junctions (**Frezza et al, 2006**). These results suggested a role for Opa1
306 in cristae junction widening in apoptosis initiation and mobilization of cytochrome c (**Scorrano et al, 2002;**
307 **Germain et al, 2005**). Here, we investigated cristae state prior to any exposure to apoptotic stimuli by
308 cryo-ET. Consistent with previous knock-down studies (**Olichon et al, 2003; Arnoult et al, 2005**), we
309 observed wider cristae junctions in Opa1-KO cells in our cryo-ET data. However, we also observed wider
310 cristae junction in s-Opa1* cells, but not in l-Opa1* cells, which have widths similar to WT. This new
311 finding suggests l-Opa1 could be the specific Opa1 form responsible for maintaining cristae junction width.
312 The presence of stable l-Opa1 population has been shown to be essential in apoptotic resistance
313 (**Merkwirth et al, 2008, 2012**). Our apoptotic priming experiments show that while s-Opa1* has similar
314 apoptotic priming to Opa1 knock-out cells, l-Opa1* cells show similar responses to WT, supporting a role
315 for l-Opa1 specifically in a cytochrome c release transition (**Merkwirth et al, 2008**).

316 Although our findings that Opa1 knock-out cells are resistant to apoptosis may seem
317 counterintuitive given previous reports of apoptotic resistance in Opa1-overexpressing cells (**Frezza et**

318 **al., 2006)**, it's important to note that Opa1 has multiple demonstrated roles in apoptosis initiation. First,
319 Opa1 maintains tight cristae junctions, and when overexpressed can lead to a further tightening of these
320 junctions, which may restrict cytochrome c release in response to pro-apoptotic signals (**Frezza et al,**
321 **2006)**. However, the importance of rearrangement and disassembly of Opa1 complexes during apoptosis
322 initiation, to facilitate crista junction opening, as discussed above, demonstrates that Opa1 also has a
323 direct role in facilitating the release of cytochrome c release when apoptosis is initiated. This view is
324 consistent with our finding that complete knock-out of Opa1 impairs cytochrome c release and can be
325 protective against apoptosis-inducing agents. Finally, since Opa1 is also necessary for mitochondrial
326 fusion, its loss leads to changes in mitochondrial morphology and size. Mitochondrial shape and the
327 curvature of the outer membrane has been previously found to affect the ability of the pro-apoptotic, pore-
328 forming protein BAX to be stabilized in the mitochondrial outer membrane and initiate mitochondrial outer
329 membrane permeabilization (MOMP) in cytochrome c release (**Renault et al, 2015)**.

330 In addition to WT-like CJ widths, we speculate that I-Opa1 maybe important in maintaining
331 perpendicular CJ, as s-Opa1* cells showed CJ with a wide range of CJ orientations, reflected by a range
332 of measured angles. Perpendicular CJs are important for facilitating cristae stacking. In our cryo-ET data,
333 we noticed a striking number of instances of stacking cristae in the I-Opa1* condition. Stacking cristae
334 have been previously observed under conditions that induce metabolic and endoplasmic reticulum stress
335 upon addition of thapsigargin (**Barad et al, 2022)**. For Opa1, processing by a stress-responsive protease
336 Oma1 would result in generation of more s-Opa1. In our experiments, the I-Opa1* condition is in a Oma1
337 ^{-/-} background, which would restrict stress-induced proteolytic processing of Opa1.

338 Our data capture a range of cristae morphological diversity. While the majority of cristae are
339 lamellar, we noticed a shift in the proportion of tubular and globular cristae in the I-Opa1* and s-Opa1*
340 cells. While tubular cristae were a notable proportion of the WT mitochondria, they were entirely absent
341 from I-Opa1* cells, but still present as a fraction of s-Opa1* cells. Tubular cristae are compatible with
342 helical assemblies of s-Opa1 and the yeast homolog, s-Mgm1, which have been visualized in membrane
343 tubes *in vitro* (**Faelber et al, 2019; Zhang et al, 2020; Hinshaw et al, 2022)**. In addition, globular cristae
344 were noticeably increased in the Opa1-KO condition, leading us to speculate the presence of either or
345 both forms of Opa1 support other alternative better-defined morphologies. Consistent with this idea, we
346 notice many instances of zipped cristae in the Opa1-OE condition.

347 We also noticed more multi-junction cristae in I-Opa1 cells. Many of these cristae fell into the
348 'straight-across' category, similar to 'septa' previously described in yeast (**Harner et al, 2016)**. In previous
349 yeast studies, septal cristae were suggested to result as a byproduct of fusion of the inner-membrane
350 (**Harner et al, 2016)**. We would expect that since I-Opa1 is required for fusion, septa would be absent
351 from the s-Opa1* condition, and indeed in s-Opa1* mitochondria we see a marked reduction of multi-

352 junction cristae. We also notice an increased IMS volume only in s-Opa1* cells. Since l-Opa1 cells have
353 IMS volumes similar to WT, this would be consistent with a role for l-Opa1 supporting an IMM-OMM
354 bridge. We also describe a class of cristae we observe as having a 'loop' morphology. This loop
355 morphology is similar to 'straight-across', but is distinguished by cristae junctions that are not at opposing
356 sides of the organelle, forcing the entire cristae to make a gradual bend.

357 We also noticed instances of cristae branching or splitting in s-Opa1* cells. Split cristae were also
358 rarely observed or not at all in Opa1-KO and l-Opa1* cristae. While a few split cristae were observed in
359 Opa1-OE, there are a considerable number of split cristae in WT and s-Opa1* cells. This may suggest s-
360 Opa1 facilitates cristae splitting and the presence of l-Opa1 regulates this function, as seen in the minimal
361 number of split cristae in Opa1-OE cells.

362 In our cryo-ET data, we also noticed differences in matrix region across the different cellular
363 conditions. We see a less condensed matrix in mitochondria in s-Opa1* cells. Because the lighter matrix
364 is also seen in the Opa1-KO mitochondria, we speculate this may be not related to apoptotic priming,
365 and instead likely due to metabolic differences. Intriguingly, we also note a fraction of Opa1-OE
366 mitochondria have empty and uneven matrices, which we speculate may be a consequence of
367 dehydration and uneven resin infiltration in the TEM samples. The 'empty' matrix phenotype was not
368 observed in wild-type, l-Opa1* or s-Opa1* cell lines. WT mitochondria had either dark or normal matrix
369 phenotypes, while the matrix in l-Opa1* and s-Opa1* cell lines appeared uneven. Interestingly, we note
370 an elevated number of mitochondria with dark matrices in the s-Opa1* cell lines. By cryo-ET, the s-Opa1*
371 matrix appeared brighter and less dense compared to the other cell lines, denoting artifacts related to
372 sample preparation for room temperature TEM imaging.

373 Since the matrix volume and cristae lumen volume together account for the majority of the
374 organelle internal volume, there is typically a trade-off between these two regions. Consistent with this
375 notion, we find in our data a reduction in matrix volume when the cristae lumen has expanded in the l-
376 Opa1*, s-Opa1*, and Opa1-KO conditions. Interestingly, histograms of cristae widths show a slight
377 reduction of the average width in s-Opa1* mitochondria. Likewise, the relative cristae lumen to matrix
378 volume in l-Opa1* cells is greater, consistent with cristae widths that are similar to WT. It is worth noting
379 that these histograms also show a distribution of cristae membrane distances, especially in the l-Opa1*,
380 Opa1-OE and Opa1-KO conditions, and the histogram peak is likely on reporting on a subset of spacings
381 along the cristae.

382 In summary, here we characterize cristae morphologies specific for the levels or forms of Opa1
383 expressed. We characterize and quantify cristae morphological differences and define distinct differences
384 specific to Opa1 form. Notably, we find evidence for l-Opa1 play important roles in maintaining CJ shape
385 and connectivity, which correlates well with WT-like apoptotic responses for cells containing mainly l-

386 Opa1. This work motivates further studies visualizing and dissecting mechanisms underlying cristae
387 lifecycles by new live cell imaging approaches to gain insight into spatio-temporal regulation of cristae
388 (**Stephan *et al*, 2019; Kleele *et al*, 2021; Zhao *et al*, 2022**). Future structural and live cell imaging studies
389 will also be necessary to directly relate how specific protein conformational states influence such
390 morphologies.

391

392 **Acknowledgments**

393 We are grateful to Phat Vinh Dip, and Edward Brignole at the MIT.nano cryo-EM facility and Kang Song
394 and Chen Xu at the University of Massachusetts cryo-EM facility for providing access to the cryo-EM
395 microscopes and for all their help, advice, and maintenance of cryo-EM equipment. Electron microscopy
396 was performed in the Microscopy Core of the Center for Systems Biology/Program in Membrane Biology,
397 which is partially supported by an Inflammatory Bowel Disease Grant DK043351 and a Boston Area
398 Diabetes and Endocrinology Research Center (BADERC) Award DK057521. We thank Connor Tou for
399 assistance cloning guide RNAs.

400

401 **Grants/funding:**

402 P.P.N. was supported by the Swiss National Science Foundation (SNF) Early Postdoc.Mobility
403 P2BSP3_188112 and Postdoc.Mobility P400PB_199252 fellowships. Z.I. was supported by NIA award
404 F32AG077861. This work was supported by a Mass General Hospital ECOR Howard M. Goodman
405 Fellowship (to B.P.K.); Charles H. Hood Foundation Child Health Research Awards to L.H.C. and K.A.S.;
406 and Alex's Lemonade Stand Foundation for Childhood Cancers Research Award to K.A.S. This work was
407 supported by funding from the National Institutes of Health (R35GM142553 to L.H.C., R01DK125263 and
408 R37CA248565 to K.A.S.

409

410 **Author Contributions**

411 P.P.N. established cryo-FIB/cryo-ET imaging and processing pipeline. P.P.N., M.Y.F., Y.G., and J.L.M.
412 acquired cryo-ET data. P.P.N and M.Y.F processed cryo-ET data and performed data analysis and
413 quantification. P.P.N and I.A. performed STA analyses. P.H., B.L., Y.G., J.L.M., L.L.H., and B.P.K
414 designed and prepared cell lines. D.C.C. generously provided the I-Opa1* and s-Opa1* cells. P.H., Y.G.
415 performed fluorescence imaging. P.P.N. trained and supported V. A. with 3D segmentation and
416 visualization of cryo-electron tomograms. V.A. performed segmentation of tomograms, subcompartment
417 volume analyses, and prepared movies. C.M.L, B.L and J.L.M performed analyses of TEM images. Z.I.,
418 X.Q., performed BH3 profiling. M.Y.F., P.P.N., V.A., P.H., B.L., L.H.C. wrote the manuscript. All authors
419 edited the manuscript.

420

421 **Declaration of Interests**

422 B.P.K is an inventor on patents and/or patent applications filed by Mass General Brigham that describe
423 genome engineering technologies. B.P.K. is a consultant for EcoR1 capital, and is an advisor to Acrogen
424 Biosciences, Life Edit Therapeutics, and Prime Medicine. The remaining authors declare that there are
425 no competing financial interests.

426 **References**

427

428 Anand R, Wai T, Baker MJ, Kladt N, Schauss AC, Rugarli E & Langer T (2014) The i-AAA protease
429 YME1L and OMA1 cleave OPA1 to balance mitochondrial fusion and fission. *J Cell Biol* 204: 919–
430 929

431 Arnoult D, Grodet A, Lee Y-J, Estaquier J & Blackstone C (2005) Release of OPA1 during Apoptosis
432 Participates in the Rapid and Complete Release of Cytochrome c and Subsequent Mitochondrial
433 Fragmentation*. *J Biol Chem* 280: 35742–35750

434 Barad BA, Medina M, Fuentes D, Wiseman RL & Grotjahn DA (2022) A surface morphometrics toolkit
435 to quantify organellar membrane ultrastructure using cryo-electron tomography. *Biorxiv*.
436 2022.01.23.477440

437 Barrera M, Koob S, Dikov D, Vogel F & Reichert AS (2016) OPA1 functionally interacts with MIC60 but
438 is dispensable for crista junction formation. *Febs Lett* 590: 3309–3322

439 Bepler T, Kelley K, Noble AJ & Berger B (2020) Topaz-Denoise: general deep denoising models for
440 cryoEM and cryoET. *Nat Commun* 11: 5208

441 Blum TB, Hahn A, Meier T, Davies KM & Kühlbrandt W (2019) Dimers of mitochondrial ATP synthase
442 induce membrane curvature and self-assemble into rows. *Proc National Acad Sci* 116: 4250–4255

443 Castaño-Díez D, Kudryashev M, Arheit M & Stahlberg H (2012) Dynamo: A flexible, user-friendly
444 development tool for subtomogram averaging of cryo-EM data in high-performance computing
445 environments. *J Struct Biol* 178: 139–151

446 Chandel NS (2014) Mitochondria as signaling organelles. *Bmc Biol* 12: 34

447 Chonghaile TN, Sarosiek KA, Vo T-T, Ryan JA, Tammareddi A, Moore VDG, Deng J, Anderson KC,
448 Richardson P, Tai Y-T, *et al* (2011) Pretreatment Mitochondrial Priming Correlates with Clinical
449 Response to Cytotoxic Chemotherapy. *Science* 334: 1129–1133

450 Cipolat S, Rudka T, Hartmann D, Costa V, Serneels L, Craessaerts K, Metzger K, Frezza C, Annaert
451 W, D’Adamio L, *et al* (2006) Mitochondrial Rhomboid PARL Regulates Cytochrome c Release
452 during Apoptosis via OPA1-Dependent Cristae Remodeling. *Cell* 126: 163–175

453 Davies KM, Anselmi C, Wittig I, Faraldo-Gómez JD & Kühlbrandt W (2012) Structure of the yeast F1Fo-
454 ATP synthase dimer and its role in shaping the mitochondrial cristae. *Proc National Acad Sci* 109:
455 13602–13607

456 Faelber K, Dietrich L, Noel JK, Wollweber F, Pfitzner A-K, Mühleip A, Sánchez R, Kudryashev M,
457 Chiaruttini N, Lilie H, *et al* (2019) Structure and assembly of the mitochondrial membrane
458 remodelling GTPase Mgm1. *Nature* 571: 429–433

459 Fraser C, Ryan J & Sarosiek K (2018) BH3 Profiling: A Functional Assay to Measure Apoptotic Priming
460 and Dependencies. *Methods Mol Biology* 1877: 61–76

- 461 Frey TG & Mannella CA (2000) The internal structure of mitochondria. *Trends Biochem Sci* 25: 319–
462 324
- 463 Frezza C, Cipolat S, Brito OM de, Micaroni M, Beznoussenko GV, Rudka T, Bartoli D, Polishuck RS,
464 Danial NN, Strooper BD, *et al* (2006) OPA1 Controls Apoptotic Cristae Remodeling Independently
465 from Mitochondrial Fusion. *Cell* 126: 177–189
- 466 Ge Y, Shi X, Boopathy S, McDonald J, Smith AW & Chao LH (2020) Two forms of Opa1 cooperate to
467 complete fusion of the mitochondrial inner-membrane. *Elife* 9: e50973
- 468 Germain M, Mathai JP, McBride HM & Shore GC (2005) Endoplasmic reticulum BIK initiates DRP1-
469 regulated remodelling of mitochondrial cristae during apoptosis. *Embo J* 24: 1546–1556
- 470 Gómez-Valadés AG, Pozo M, Varela L, Boudjadja MB, Ramírez S, Chivite I, Eyre E, Haddad-Tóvulli R,
471 Obri A, Milà-Guasch M, *et al* (2021) Mitochondrial cristae-remodeling protein OPA1 in POMC
472 neurons couples Ca²⁺ homeostasis with adipose tissue lipolysis. *Cell Metab* 33: 1820-1835.e9
- 473 Hagen WJH, Wan W & Briggs JAG (2017) Implementation of a cryo-electron tomography tilt-scheme
474 optimized for high resolution subtomogram averaging. *J Struct Biol* 197: 191–198
- 475 Harner ME, Unger A-K, Geerts WJ, Mari M, Izawa T, Stenger M, Geimer S, Reggiori F, Westermann B
476 & Neupert W (2016) An evidence based hypothesis on the existence of two pathways of
477 mitochondrial crista formation. *Elife* 5: e18853
- 478 Hashimi H (2019) A parasite's take on the evolutionary cell biology of MICOS. *Plos Pathog* 15:
479 e1008166
- 480 Hinshaw J, Nyenhuis S, Wu X, Stanton A, Strub M-P, Yim Y-I & Canagarajah B (2022) Opa1 helical
481 structures give perspective to mitochondrial dysfunction.
- 482 Kleele T, Rey T, Winter J, Zaganelli S, Mahecic D, Lambert HP, Ruberto FP, Nemir M, Wai T,
483 Pedrazzini T, *et al* (2021) Distinct fission signatures predict mitochondrial degradation or biogenesis.
484 *Nature* 593: 435–439
- 485 Kremer JR, Mastronarde DN & McIntosh JR (1996) Computer Visualization of Three-Dimensional
486 Image Data Using IMOD. *J Struct Biol* 116: 71–76
- 487 Mahamid J, Pfeffer S, Schaffer M, Villa E, Danev R, Cuellar LK, Förster F, Hyman AA, Plitzko JM &
488 Baumeister W (2016) Visualizing the molecular sociology at the HeLa cell nuclear periphery.
489 *Science* 351: 969–972
- 490 Mannella CA (2006) Structure and dynamics of the mitochondrial inner membrane cristae. *Biochimica
491 Et Biophysica Acta Bba - Mol Cell Res* 1763: 542–548
- 492 Martinez-Sanchez A, Garcia I, Asano S, Lucic V & Fernandez J-J (2014) Robust membrane detection
493 based on tensor voting for electron tomography. *J Struct Biol* 186: 49–61
- 494 Mastronarde DN (2003) SerialEM: A Program for Automated Tilt Series Acquisition on Tecnai
495 Microscopes Using Prediction of Specimen Position. *Microsc Microanal* 9: 1182–1183

- 496 Mastronarde DN & Held SR (2017) Automated tilt series alignment and tomographic reconstruction in
497 IMOD. *J Struct Biol* 197: 102–113
- 498 Merkwirth C, Dargazanli S, Tatsuta T, Geimer S, Löwer B, Wunderlich FT, Kleist-Retzow J-C von,
499 Waisman A, Westermann B & Langer T (2008) Prohibitins control cell proliferation and apoptosis by
500 regulating OPA1-dependent cristae morphogenesis in mitochondria. *Gene Dev* 22: 476–488
- 501 Merkwirth C, Martinelli P, Korwitz A, Morbin M, Brönneke HS, Jordan SD, Rugarli EI & Langer T (2012)
502 Loss of Prohibitin Membrane Scaffolds Impairs Mitochondrial Architecture and Leads to Tau
503 Hyperphosphorylation and Neurodegeneration. *Plos Genet* 8: e1003021
- 504 Mishra P, Carelli V, Manfredi G & Chan DC (2014) Proteolytic Cleavage of Opa1 Stimulates
505 Mitochondrial Inner Membrane Fusion and Couples Fusion to Oxidative Phosphorylation. *Cell Metab*
506 19: 630–641
- 507 Mishra P & Chan DC (2016) Metabolic regulation of mitochondrial dynamics. *J Cell Biol* 212: 379–387
- 508 Navarro P, Scaramuzza S, Stahlberg H & Castaño-Díez D (2020) The Dynamo Software Package for
509 Cryo-electron Tomography and Subtomogram Averaging. *Microsc Microanal* 26: 3142–3145
- 510 Navarro PP, Stahlberg H & Castaño-Díez D (2018) Protocols for Subtomogram Averaging of
511 Membrane Proteins in the Dynamo Software Package. *Frontiers Mol Biosci* 5: 82
- 512 Navarro PP, Vettiger A, Ananda VY, Llopis PM, Allolio C, Bernhardt TG & Chao LH (2022) Cell wall
513 synthesis and remodelling dynamics determine division site architecture and cell shape in
514 *Escherichia coli*. *Nat Microbiol* 7: 1621–1634
- 515 Olichon A, Baricault L, Gas N, Guillou E, Valette A, Belenguer P & Lenaers G (2003) Loss of OPA1
516 Perturbates the Mitochondrial Inner Membrane Structure and Integrity, Leading to Cytochrome c
517 Release and Apoptosis*. *J Biol Chem* 278: 7743–7746
- 518 Pettersen EF, Goddard TD, Huang CC, Couch GS, Greenblatt DM, Meng EC & Ferrin TE (2004) UCSF
519 Chimera—A visualization system for exploratory research and analysis. *J Comput Chem* 25: 1605–
520 1612
- 521 Picard M & Shirihai OS (2022) Mitochondrial signal transduction. *Cell Metab* 34: 1620–1653
- 522 Renault TT, Floros KV, Elkholi R, Corrigan K-A, Kushnareva Y, Wieder SY, Lindtner C, Serasinghe MN,
523 Ascioffa JJ, Buettner C, *et al* (2015) Mitochondrial Shape Governs BAX-Induced Membrane
524 Permeabilization and Apoptosis. *Mol Cell* 57: 69–82
- 525 Rigort A, Bäuerlein FJB, Villa E, Eibauer M, Laugks T, Baumeister W & Plitzko JM (2012) Focused ion
526 beam micromachining of eukaryotic cells for cryoelectron tomography. *Proc National Acad Sci* 109:
527 4449–4454
- 528 Sarosiek KA, Fraser C, Muthalagu N, Bhola PD, Chang W, McBrayer SK, Cantlon A, Fisch S, Golomb-
529 Mello G, Ryan JA, *et al* (2017) Developmental Regulation of Mitochondrial Apoptosis by c-Myc
530 Governs Age- and Tissue-Specific Sensitivity to Cancer Therapeutics. *Cancer Cell* 31: 142–156

- 531 Schagger H & Pfeiffer K (2000) Supercomplexes in the respiratory chains of yeast and mammalian
532 mitochondria. *Embo J* 19: 1777–1783
- 533 Schindelin J, Arganda-Carreras I, Frise E, Kaynig V, Longair M, Pietzsch T, Preibisch S, Rueden C,
534 Saalfeld S, Schmid B, *et al* (2012) Fiji: an open-source platform for biological-image analysis. *Nat*
535 *Methods* 9: 676–682
- 536 Scorrano L, Ashiya M, Buttle K, Weiler S, Oakes SA, Mannella CA & Korsmeyer SJ (2002) A Distinct
537 Pathway Remodels Mitochondrial Cristae and Mobilizes Cytochrome c during Apoptosis. *Dev Cell* 2:
538 55–67
- 539 Song Z, Chen H, Fiket M, Alexander C & Chan DC (2007) OPA1 processing controls mitochondrial
540 fusion and is regulated by mRNA splicing, membrane potential, and Yme1L. *J Cell Biology* 178:
541 749–755
- 542 Spetz JKE, Florido MHC, Fraser CS, Qin X, Choiniere J, Yu SJ, Singh R, Friesen M, Rubin LL, Salem
543 J-E, *et al* (2022) Heightened apoptotic priming of vascular cells across tissues and life span
544 predisposes them to cancer therapy–induced toxicities. *Sci Adv* 8: eabn6579
- 545 Spinelli JB & Haigis MC (2018) The multifaceted contributions of mitochondria to cellular metabolism.
546 *Nat Cell Biol* 20: 745–754
- 547 Stephan T, Roesch A, Riedel D & Jakobs S (2019) Live-cell STED nanoscopy of mitochondrial cristae.
548 *Sci Rep-uk* 9: 12419
- 549 Strubbe-Rivera JO, Schrad JR, Pavlov EV, Conway JF, Parent KN & Bazil JN (2021) The mitochondrial
550 permeability transition phenomenon elucidated by cryo-EM reveals the genuine impact of calcium
551 overload on mitochondrial structure and function. *Sci Rep-uk* 11: 1037
- 552 Twig G, Elorza A, Molina AJA, Mohamed H, Wikstrom JD, Walzer G, Stiles L, Haigh SE, Katz S, Las G,
553 *et al* (2008) Fission and selective fusion govern mitochondrial segregation and elimination by
554 autophagy. *Embo J* 27: 433–446
- 555 Wagner FR, Watanabe R, Schampers R, Singh D, Persoon H, Schaffer M, Fruhstorfer P, Plitzko J &
556 Villa E (2020) Preparing samples from whole cells using focused-ion-beam milling for cryo-electron
557 tomography. *Nat Protoc* 15: 2041–2070
- 558 Walton RT, Christie KA, Whittaker MN & Kleinstiver BP (2020) Unconstrained genome targeting with
559 near-PAMless engineered CRISPR-Cas9 variants. *Science* 368: 290–296
- 560 Wang R, Mishra P, Garbis SD, Moradian A, Sweredoski MJ & Chan DC (2021) Identification of new
561 OPA1 cleavage site reveals that short isoforms regulate mitochondrial fusion. *Mol Biol Cell* 32: 157–
562 168
- 563 Wolf SG, Mutsafi Y, Dadosh T, Ilani T, Lansky Z, Horowitz B, Rubin S, Elbaum M & Fass D (2017) 3D
564 visualization of mitochondrial solid-phase calcium stores in whole cells. *Elife* 6: e29929

- 565 Wolff G, Limpens RWAL, Zheng S, Snijder EJ, Agard DA, Koster AJ & Bárcena M (2019) Mind the gap:
566 Micro-expansion joints drastically decrease the bending of FIB-milled cryo-lamellae. *J Struct Biol*
567 208: 107389
- 568 Yang R, Zhao G, Liang S, Zhang Y, Sun L, Chen H & Liu D (2012) Mitofilin regulates cytochrome c
569 release during apoptosis by controlling mitochondrial cristae remodeling. *Biochem Bioph Res Co*
570 428: 93–98
- 571 Zhang D, Zhang Y, Ma J, Zhu C, Niu T, Chen W, Pang X, Zhai Y & Sun F (2020) Cryo-EM structures of
572 S-OPA1 reveal its interactions with membrane and changes upon nucleotide binding. *Elife* 9:
573 e50294
- 574 Zhao Y, Zhang M, Zhang W, Zhou Y, Chen L, Liu Q, Wang P, Chen R, Duan X, Chen F, *et al* (2022)
575 Isotropic super-resolution light-sheet microscopy of dynamic intracellular structures at subsecond
576 timescales. *Nat Methods* 19: 359–369
- 577 Zick M, Rabl R & Reichert AS (2009) Cristae formation—linking ultrastructure and function of
578 mitochondria. *Biochimica Et Biophysica Acta Bba - Mol Cell Res* 1793: 5–19
- 579

580 **Methods**

581

582 **Cell lines and culture**

583 MEFs were maintained in DMEM supplemented with 10% fetal bovine serum (FBS) and 1%
584 penicillin/streptomycin at 37°C and 5% CO₂. Wildtype and Opa1 knock-out MEF cell lines were purchased
585 from ATCC. Δ *exon5b/Oma1*-null cells and Opa1 knock-outs transfected with Opa1 Isoform 5 (KO Opa1
586 + Iso5) were kind gifts from David Chan (California Institute of Technology). The KO Opa1 + Iso5 were
587 maintained in the same condition described above and supplemented with puromycin at 1µg/mL for
588 selection. Cell genotypes were confirmed by Western blotting.

589

590 To generate Opa1 overexpressing MEFs, wildtype MEFs were transiently transfected with pMSCV-Opa1,
591 a kind gift from David Chan (Addgene plasmid #26047; <http://n2t.net/addgene:26047>;
592 RRID:Addgene_26047). The transfected cells were selected with 5 µg/mL puromycin 24 h after
593 transfection for 14 days. Clones were expanded for 3 days, and their genotypes were confirmed by
594 Western blotting.

595

596 Human HEK 293T cells (American Type Culture Collection; ATCC) were cultured in Dulbecco's Modified
597 Eagle Medium (DMEM) supplemented with 10% heat-inactivated FBS (HI-FBS) and 1% penicillin-
598 streptomycin. Samples of supernatant media from cell culture experiments were analyzed monthly for
599 the presence of mycoplasma using MycoAlert PLUS (Lonza).

600

601 To generate a HEK 293T cell line bearing an *OPA1* exon 5b knock-out, SpCas9 sgRNAs were cloned
602 into pUC19-U6-BsmBI_cassette-SpCas9gRNA (BPK1520; Addgene ID 65777) harboring spacer
603 sequences GCTCATTGTGAACTCGTGGCA (plasmid CJT90), GCCAACAGAAGCGCAAGGTGA
604 (plasmid CJT91), GTTCTCCTCATTGTGAACTCG (plasmid CJT92), and
605 GCAGAAGCGCAAGGTGATGGA (plasmid CJT93), each with added 5'Gs. Transfections were
606 performed 20 hours following seeding of 2x10⁴ HEK 293T cells per well in 96-well plates. Transfections
607 contained 70 ng of SpCas9 nuclease plasmid (pCMV-T7-SpCas9-P2A-EGFP (RTW3027; Addgene ID
608 139987) and 15 ng each of two sgRNA expression plasmids mixed with 0.3 µL of TransIT-X2 (Mirus) in
609 a total volume of 15 µL Opti-MEM (Thermo Fisher Scientific), incubated for 15 minutes at room
610 temperature, and distributed across the seeded HEK 293T cells. Cells were grown for approximately 72
611 hours prior to extracting genomic DNA (gDNA) by discarding the media, resuspending the cells in 100
612 µL of quick lysis buffer (20 mM Hepes pH 7.5, 100 mM KCl, 5 mM MgCl₂, 5% glycerol, 25 mM DTT, 0.1%
613 Triton X-100, and 60 ng/µL Proteinase K (New England Biolabs; NEB)), heating the lysate for 6 minutes

614 at 65 °C, heating at 98 °C for 2 minutes, and then storing at -20 °C. Editing efficiency in bulk transfected
615 cells was assessed by next-generation sequencing (NGS) essentially as previously described (Walton *et*
616 *al*, 2020) using PCR round 1 primers oLLH9-
617 ACACTCTTCCCTACACGACGCTCTTCCGATCTCATCTGTTCCCTTGTGACACCCTTGG and
618 oLLH10-GACTGGAGTTCAGACGTGTGCTCTTCCGATCTGGAGTCCATGAACAGATTGAGGTGAC.
619 To create cell lines, HEK 293T cells were seeded and transfected with plasmids RTW3027 and both
620 sgRNAs CJT91 and CJT92. Transfected cells were grown for approximately 72 hours prior to dilution
621 plating into 96-well plates and grown until confluent. Cells were transferred into 24-well plates with some
622 cell mass reserved to extract genomic DNA (gDNA) for genotyping via PCR and NGS to verify biallelic
623 *OPA1* exon 5b deletion between the two SpCas9-sgRNA cleavage sites.

624

625 To generate a HEK 293T cell line bearing an *OPA1* R194G mutation, SpCas9 sgRNAs were cloned into
626 BPK1520 harboring spacer sequences GCGGCGTTTAGAGCAACAGAT (plasmid CJT87),
627 GCGTTTAGAGCAACAGATCGT (plasmid CJT88), and GCGTTTAGAGCAACAGATCG (plasmid
628 CJT89). Adenine base editor (ABE) plasmids included pCMV-T7-ABE8e-nSpCas9-P2A-EGFP (KAC978;
629 Addgene ID 185910) or pCMV-T7-ABE8e-nSpG-P2A-EGFP (KAC984; Addgene ID 185911).
630 Transfections were performed 20 hours following seeding of 2x10⁴ HEK 293T cells per well in 96-well
631 plates and contained 70 ng of ABE8e plasmid and 30 ng of sgRNA expression plasmid mixed with 0.3
632 µL of TransIT-X2 (Mirus) in a total volume of 15 µL Opti-MEM (Thermo Fisher Scientific). The transfection
633 mixtures were incubated for 15 minutes at room temperature and distributed across the seeded HEK
634 293T cells. Cells were grown for approximately 72 hours prior to extracting gDNA as described above.
635 Editing efficiency in bulk transfected cells was assessed by NGS using PCR round 1 primers oLLH7-
636 ACACTCTTCCCTACACGACGCTCTTCCGATCTGCTTAGGCTGTTGACATCACTGGAGAATG and
637 oLLH8-GACTGGAGTTCAGACGTGTGCTCTTCCGATCTCCAGAACTGCCACGTAATACCTTGTAC. To
638 create cell lines, HEK 293T cells were seeded and transfected with plasmids KAC984 and CJT88.
639 Transfected cells were grown for approximately 72 hours prior to dilution plating into 96-well plates and
640 grown until confluent. Cells were transferred into 24-well plates with some cell mass reserved to extract
641 genomic DNA (gDNA) for genotyping via PCR and NGS to verify biallelic introduction of *OPA1*-R194G.

642

643 **Live cell fluorescence microscopy**

644 Confluent MEF cells were harvested, seeded onto 35 mm glass-bottom dishes (MatTek Life Sciences)
645 coated with poly-D-lysine (0.1 mg/mL) and allowed to grow overnight at 37°C under 5% CO₂. For
646 visualization of mitochondria, cells were stained with 50nM MitoTracker™ Deep Red FM (Thermo Fisher
647 Scientific) at 37°C for 15 mins. Following three rounds of washes with 1X PBS, cells were placed in Live

648 Cell Imaging Solution (Invitrogen). All fluorescence imaging was performed using Zeiss Axio Observer
649 Z1 Advanced Marianas™ Microscope system, an Alpha Plan-Apochromat 100x/1.46 NA Oil TIRF
650 Objective M27 and Prime 95B scientific CMOS camera (Photometrics). MitoTracker™-stained
651 mitochondria were imaged using “Cy5” filter set (Cy5-4040C, Excitation: 628/40 nm [608-648nm],
652 Emission: 692/40 nm [672-712nm], Dichroic Mirror: 660nm) (Semrock). Temperature, humidity, and CO₂
653 concentrations were controlled with an Okolab Microscope Stage Incubator System. Image acquisition
654 and processing were done using SlideBook™6 (Intelligent Imaging Innovations, Inc, Denver, CO) and Fiji
655 (Schindelin et al., 2012). Time-lapse videos of stained mitochondria were taken at one frame per 30
656 seconds for a duration of 5 mins.

657

658 **TEM fixed/stained image quantification and phenotype classification**

659 Growth media was decanted from culture dishes followed by the immediate addition of a modified
660 Karnovsky's solution (2% paraformaldehyde/2.5% glutaraldehyde in 0.1M sodium cacodylate buffer (pH
661 7.4, Electron Microscopy Sciences, Hatfield, PA); fixative was allowed to infiltrate for at least 2 hr with
662 dishes on a gentle rotator at room temperature, then stored overnight with cells in fresh fixative at 4°C.
663 The following day, fixative was decanted, cells rinsed with several exchanges of 0.1M cacodylate buffer,
664 then dishes scraped and suspensions pelleted (2500 rpm for 20min @ 4°C). Pelleted material was post-
665 fixed 1hr in 1% osmium tetroxide/0.1M cacodylate buffer, rinsed thoroughly in 0.1M cacodylate buffer,
666 then embedded in 2% agarose to stabilize aggregate. Small blocks of agarose-embedded cells were
667 dehydrated through a graded series of ethanol to 100%, dehydrated briefly in 100% propylene oxide,
668 then allowed to pre-infiltrate in a 1:1 mix of propylene oxide and Eponate resin (Ted Pella, Redding, CA)
669 overnight at room temperature on a gentle rotator. Samples were transferred into freshly prepared 100%
670 Eponate resin the following day, allowed to infiltrate several more hours, then embedded in labeled flat
671 molds in 100% fresh Eponate resin and allowed to polymerize 24-48hrs at 60°C.
672 Thin (70nm) sections were cut using a Leica EM UC7 ultramicrotome, collected onto formvar-coated
673 grids, stained with 2% uranyl acetate and Reynold's lead citrate and examined in a JEOL JEM 1011
674 transmission electron microscope at 80 kV. Images were collected using an AMT digital imaging system
675 with proprietary image capture software (Advanced Microscopy Techniques, Danvers, MA).
676 Images acquired through TEM were quantified using Fiji (**Schindelin et al, 2012**). A scale was set for
677 each magnification using a calibrated scale bar. Cell size was measured through images acquired at
678 x3000-x20,000 magnification meanwhile mitochondrial number and size were measured through images
679 acquired at x30,000-x60,000 magnification. Cell area was first selected and measured in images at lower
680 magnification. Mitochondria were selected based on the visibility of a double membrane in images at

681 higher magnification. Some unclear cellular structures were noted, but not included in the quantification
682 as mitochondria. Numbers of mitochondria were recorded, and total area was measured in μm^2 .
683 Each mitochondrion from the initial quantification was further analyzed by examining individual
684 morphologies and categorizing mitochondria into phenotype classes based on their appearance at higher
685 magnification TEM images. Separate phenotype classes were determined for mitochondrion shape,
686 cristae morphology and matrix appearance. The classes were informed partly from literature (Stephan et
687 al., 2020) and from overview qualitative analysis of phenotypes seen in the many mitochondria in this
688 study.

689

690 **Cryo-EM specimen preparation**

691 Cells were prepared following the deposition method. Cells were detached and counted with a
692 hemocytometer. Quantifoil 200 mesh holey carbon R2/2 (EMS) were glow-discharged for 60s or 90s at
693 20mA or 15mA using a PELCO easiGlow glow discharge system (Ted Pella). ~1000-3000 cells were
694 deposited onto a grid by pipetting 3 μL of detached cells onto the EM grid. Blotting and plunging was
695 performed in a FEI Vitrobot Mark IV (Thermo Fisher Scientific, here-inafter TFS) at RT, 100% humidity
696 with a waiting time of 60 seconds, one-side blotting time of 15 seconds and blotting force of 10 or 7.
697 Customized parafilm sheets were used for one-sided blotting. All subsequent grid handling and transfers
698 were performed in liquid nitrogen. Grids were clipped onto cryo-FIB autogrids (TFS).

699

700 **Cryo-FIB milling**

701 Grids were loaded in an Aquilos 2 Cryo-FIB (TFS). Specimen was sputter coated inside the cryo-FIB
702 chamber with inorganic platinum, an integrated gas injection system (GIS) was used to deposit an
703 organometallic platinum layer to protect the specimen surface and avoid uneven thinning of cells
704 (**Wagner et al, 2020**). Cryo-FIB milling was performed on the specimen using two rectangular patterns
705 to mill top and bottom parts of cells, and two extra rectangular patterns were used to create macro-
706 expansion joints to improve lamellae instability (**Wolff et al, 2019**). Cryo-FIB was performed at a nominal
707 tilt angle of 14-26 which translates into a milling angle of 7-19. Cryo-FIB milling was performed in several
708 steps of decreasing ion beam current ranging from 1 nA to 10 pA and decreasing thickness to obtain
709 200-400 nm lamellae.

710

711 **Cryo-electron tomography**

712 All imaging was performed on a FEI Titan Krios (TFS) transmission electron microscope operated at
713 300KeV equipped with a Gatan BioQuantum K3 energy filter (20eV zero-loss filtering and a Gatan K3
714 direct electron detector. Prior acquisition, a full K3 gain reference was acquired, and ZLP and

715 BioQuantum energy filter were finely tuned. The nominal magnification for data collection was 33,000x
716 giving a calibrated 4K pixel size of 2.758. Data collection was performed in nanoprobe mode using
717 SerialEM (**Mastronarde, 2003**) or TFS Tomography 6 software. The tilt range varied depending on the
718 lamella, but generally was from -70 to 70 in 2 steps following the dose-symmetric scheme (**Hagen et al,**
719 **2017**). Tilt images were acquired as 8K x 11K super-resolution movies of 6 frames with a set dose rate
720 of 1.5-3 e-/Å/sec. Tilt series were collected at a range of nominal defoci between -1 and -6 μm and a
721 target total dose of 100 to 180 e-/Å (Supplementary Table 1).

722

723 **Cryo-electron tomography image processing**

724 Acquired tilted super-resolution movies were motion corrected and Fourier cropped to 4K x 5K stacks,
725 minimizing aliasing effects using *framealign* from IMOD (**Kremer et al, 1996**). Tilt-series were aligned
726 using etomo in IMOD (**Mastronarde & Held, 2017**). CTF-estimation was performed in IMOD (**Turoňová**
727 **et al, 2017**) and/or using customized MATLAB scripts. CTF-correction was performed by *ctfphaseflip*
728 program in IMOD. CTF-corrected unbinned tomograms were reconstructed by weighted back projection
729 with and without a SIRT-like filter and subsequently 2x, 4x and 8x in IMOD. Cryo-electron tomograms
730 were denoised using Topaz (**Bepler et al, 2020**) and summed projection of cryo-tomogram slices were
731 performed in *Dynamo* (**Castaño-Díez et al, 2012**) complemented with customized MATLAB scripts.

732

733 **3D Segmentation**

734 Segmentation was done in TomoSegMemTV (**Martinez-Sanchez et al, 2014**) to create the first
735 triangulation of mitochondrial membranes. Such triangulation was refined using Amira (TFS) by unbiased
736 semi-automatic approaches. Final triangulated surfaces were remeshed and smooth in Amira for final
737 rendering.

738

739 **Quantitative analysis of cryo-ET data**

740 *Mitochondrial shape:* Mitochondria morphology was categorized into 'ellipsoidal', 'round', 'heart-shaped'
741 (when displaying a polygon shape) and 'partial' (when mitochondria was out of the XY image) by visual
742 inspection of cryo-electron tomograms.

743

744 *Mitochondrial size:* Mitochondria were outlined in summed projection images of the central slices of cryo-
745 electron tomograms in FIJI using the 'polygon selection' tool and pressing the measure key to output the
746 area of outline mitochondria in nm²

747

748 *Mitochondrial coverage*: Mitochondria area in μm^2 obtained from mitochondria size measurements was
749 divided by the total area of the summed projected image.

750

751 *Matrix density*: Mitochondria density was measured in summed projection images of the central slices of
752 cryo-electron tomograms that were all equally grey scale normalized in FIJI by applying the function
753 equalize histogram set at 0.35% for all images. Three lines were drawn in the matrix region of the
754 mitochondria under analysis and their mean grey value was calculated by pressing the measure button
755 in FIJI (**Schindelin et al, 2012**). Three measurements per mitochondria were obtained, thus, the mean
756 was calculated to obtain a single value per mitochondrial matrix.

757

758 *Cristae density*: Number of cristae was quantified in cryo-electron tomogram using the multi-point tool in
759 FIJI. The number of cristae was normalized against area of mitochondria in μm^2 .

760

761 *Mitochondrial volume*: Total mitochondria volume was calculated in Amira by summing the volume of
762 cristae lumen (CL), inter membrane spacing (IMS) and matrix volume in μm^3 . CL, IMS and matrix volumes
763 was outputted by Amira based on the 3D surface of each compartment segmented and rendered in Amira
764 with the module 'measure surface'. Ratios were calculated by dividing the volume values of the specified
765 mitochondrial compartments.

766

767 *Cristae directionality*: Cristae was classified as 'straight', 'tilted' or 'disconnected' by visual inspection of
768 cryo-electron tomograms.

769

770 *Cristae shape*: Cristae was classified as 'lamellar', 'globular', 'tubular' or 'unusual' by visual inspection of
771 cryo-electron tomograms. Within the category 'unusual' the following classes were defined: 'loop' when
772 cristae present two cristae connection with the IMS and was curved, 'pinching' when cristae membranes
773 presenting punctual touching points, 'straight-across' when cristae present two cristae connection with
774 the IMS just opposite to each other forming a straight septum-like structure across a mitochondrion,
775 'amorphous' when cristae displayed an irregular polygon shape, 'splitting' when cristae branched into two
776 or more cristae within a giving mitochondrion, 'ring' when cristae formed a circular ring within mitochondria,
777 'zip' when cristae membranes come close and only one membrane was distinguished that later opens up
778 into regular lamellar cristae, and 'vesicular' when cristae was wide, usually amorphous, but contained
779 electron dense material resembling to membranes.

780

781 *Cristae length*

782 Cristae length was measured in cryo-electron tomograms by extracting the cristae volumes in *Dynamo*
783 using the 'oblique slices in tomoslice' tool
784 (https://wiki.dynamo.biozentrum.unibas.ch/w/index.php/Oblique_slices_in_tomoslice). Then, length was
785 computing using the length tool in *Dynamo*
786 ([https://wiki.dynamo.biozentrum.unibas.ch/w/index.php/Walkthrough_on_GUI_based_tilt_series_alignm](https://wiki.dynamo.biozentrum.unibas.ch/w/index.php/Walkthrough_on_GUI_based_tilt_series_alignment_(EMBO2021)#Visualization_matrix)
787 [ent \(EMBO2021\)#Visualization_matrix](https://wiki.dynamo.biozentrum.unibas.ch/w/index.php/Walkthrough_on_GUI_based_tilt_series_alignment_(EMBO2021)#Visualization_matrix)).

788

789 *Cristae width*

790 Subtomogram averaging was performed in *Dynamo*. Particles were identified using 'dtmslice' interface
791 in *Dynamo* (Navarro *et al*, 2018, 2020). Subtomograms with a size of $(1058.8)^3$ Å were extracted from
792 4x-binned tomograms. A starting reference generated from a random set of particles was used for 3D
793 particle alignment. A total of 12 iterations were used to align particles until convergence, i.e., until no
794 further improvement of alignment parameters was detected by additional iterations, and then final
795 averages were obtained. Final averages were generated from 222 (WT), 430 (OE-Opa1), 323 I-Opa1*,
796 653 s-Opa1* and 243 KO-Opa1 subtomograms. EM densities were visualized in UCSF Chimera
797 (Pettersen *et al*, 2004). Per particle 3D width measurement was done in *Dynamo* by cross-correlation of
798 each particle against a set of 40 templates displaying a distance range between membranes of 1 to 40
799 pixels (corresponding to 2.2 to 88 nm distance,
800 [https://wiki.dynamo.biozentrum.unibas.ch/w/index.php/Framework_for_estimation_of_membrane_thick](https://wiki.dynamo.biozentrum.unibas.ch/w/index.php/Framework_for_estimation_of_membrane_thickness)
801 [ness](https://wiki.dynamo.biozentrum.unibas.ch/w/index.php/Framework_for_estimation_of_membrane_thickness)). Cross-correlation peak per particle correspond to the distance value between the two cristae
802 membranes defined here as cristae width (Fig. S6).

803

804 *Cristae junction measurement*

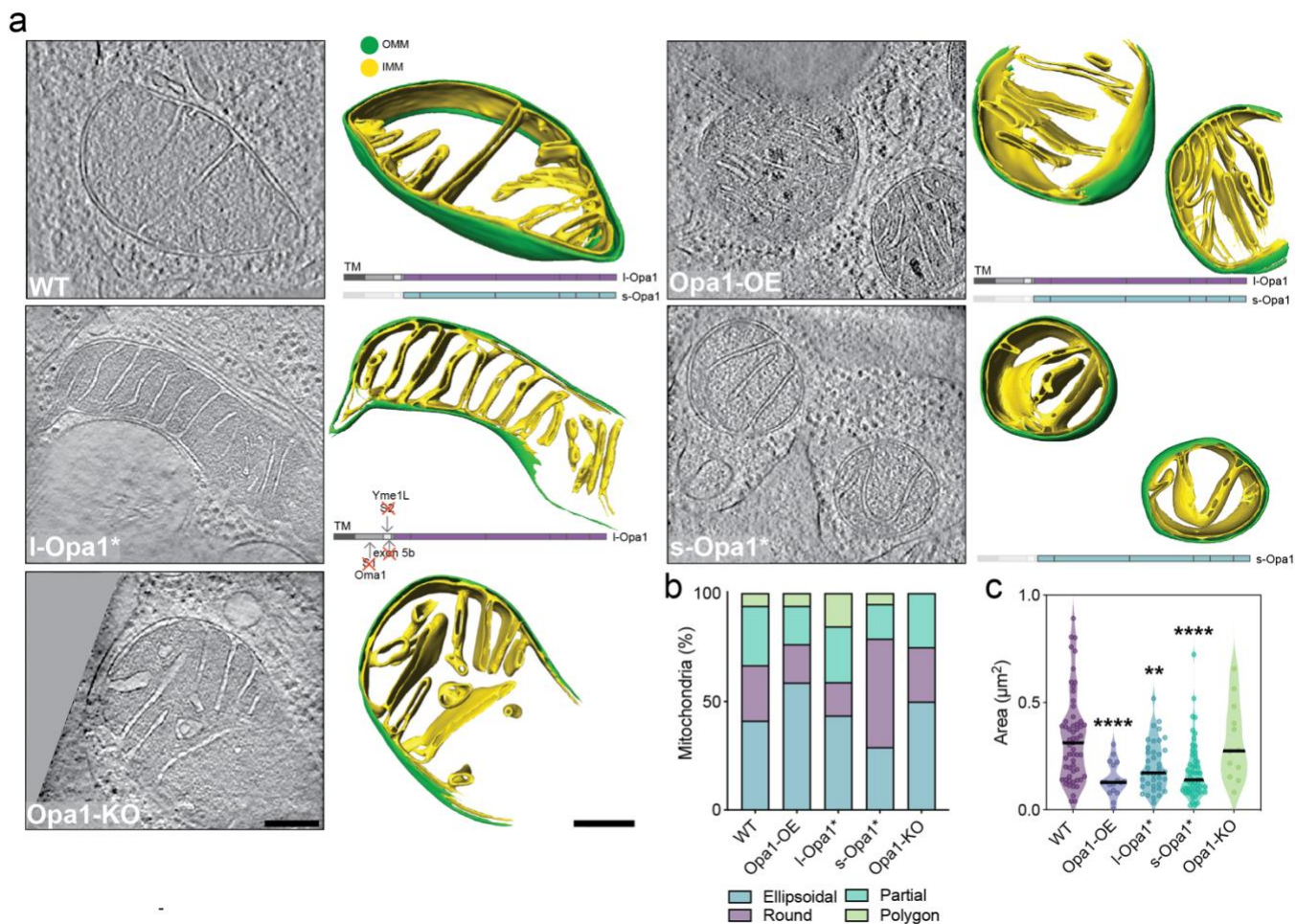
805 Cristae junctions were measured in summed projection images of 10 slices from each tomogram. Each
806 CJ was isolated and the width was measured using the line tool and measurement function in FIJI
807 (Schindelin *et al*, 2012). The angle of each CJ was measured using the angle tool and measure function
808 in FIJI. If a CJ was visible in multiple and nonoverlapping sections of the tomograms, multiple
809 measurements were made for that CJ and averaged to represent the overall 3D shape of the CJ.

810

811 **BH3 profiling and chemosensitivity methods**

812 BH3 profiling was conducted by flow cytometry according to published protocols (PMID: 30535998).
813 Briefly, cells in culture were trypsinized and added to wells of prepared 96 well plates containing the
814 indicated peptide conditions and .001% digitonin in mannitol experimental buffer (MEB; 10 mM HEPES
815 (pH 7.5), 150 mM mannitol, 50 mM KCl, 0.02 mM EGTA, 0.02 mM EDTA, 0.1% BSA, and 5 mM

816 succinate). Peptide treatments were carried out for 60 minutes at 28 degrees C, then cells were fixed
817 for 10 minutes in 2% PFA. Fixation was quenched with N2 buffer (1.7 M tris base and 1.25 M glycine
818 (pH 9.1)), then cells were stained overnight with DAPI and an Alexa Fluor 647-conjugated anti-
819 cytochrome c antibody (Biolegend, clone 6H2.B4). Stained cells were analyzed using an Attune NxT
820 flow cytometer, with gates drawn based on cytochrome c staining in the negative and positive control
821 treatments (DMSO and DFNA5 peptide). The percentage of cytochrome c negative cells was reported
822 for each peptide treatment condition.



823

824 **Figure 1 | *In situ* mitochondrial membrane morphology is influenced by Opa1 processing.**

825 Mitochondria with distinguishable inner mitochondrial membrane (IMM) and outer mitochondrial

826 membrane (OMM) visualized by cryo-ET. **(a)** (Right) Summed, projected central slices of cryo-electron

827 tomograms visualizing representative mitochondria in indicated MEF lines. (Left) Three-dimensional (3D)

828 rendering of segmented membranes with mitochondria shown across Z slices. Green and yellow surfaces

829 indicate OMM and IMM, respectively. (Bottom left) Schematic of Opa1 forms present in respective cell

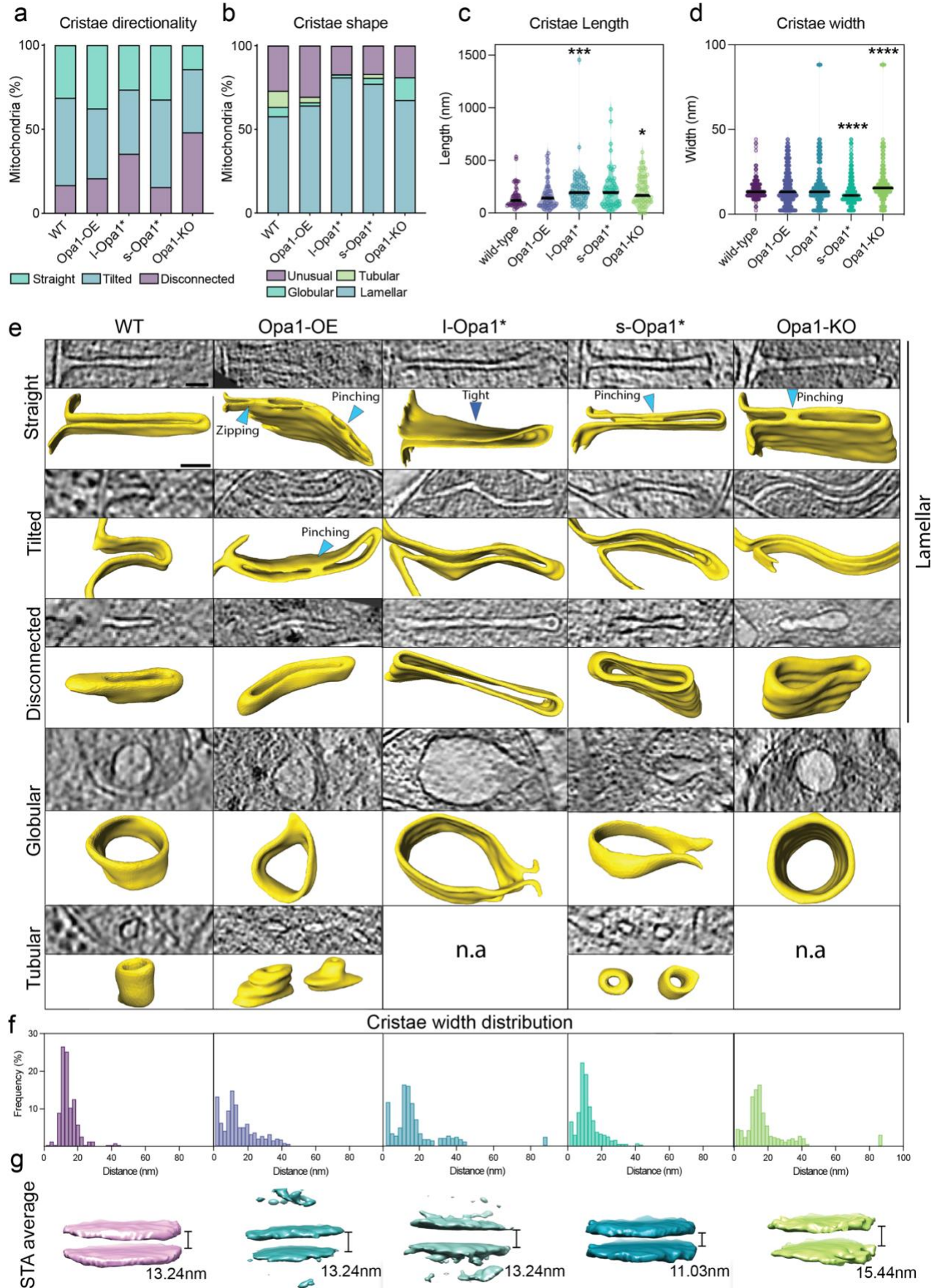
830 lines. **(b)** Graph bar representing the relative proportion of different mitochondrial shapes observed. **(c)**

831 Plot of mitochondria size (μm^2) observed in cryo-electron tomograms in MEF lines. Violin graphs show

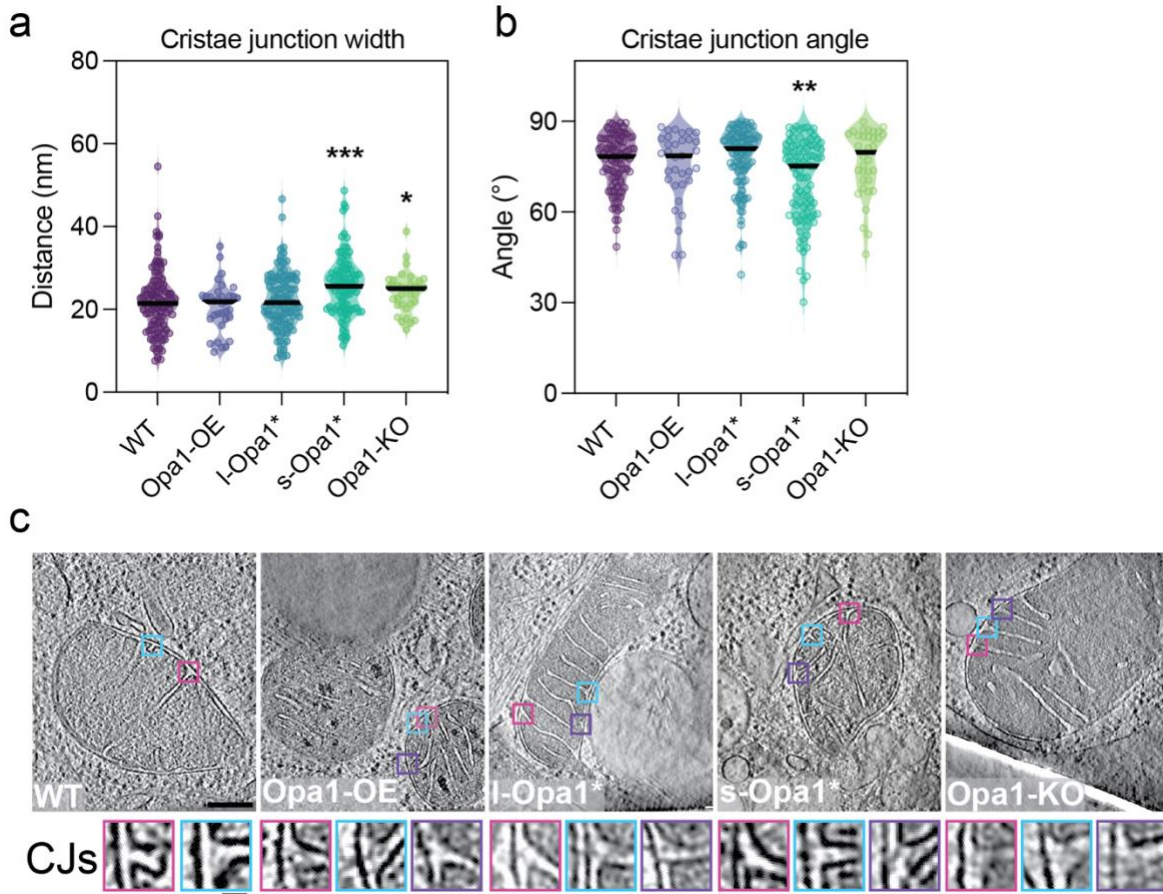
832 data distribution, the mean is shown by a bold black line. Significance of difference is tested relative to

833 wild type using Mann Whitney test; * $p < 0.05$, ** $p < 0.01$, **** $p < 0.0001$. N: wild-type = 57, Opa1-OE = 17, I-

834 Opa1* = 39, s-Opa1* = 55, Opa1-KO = 12. Scale bar = 200 nm.

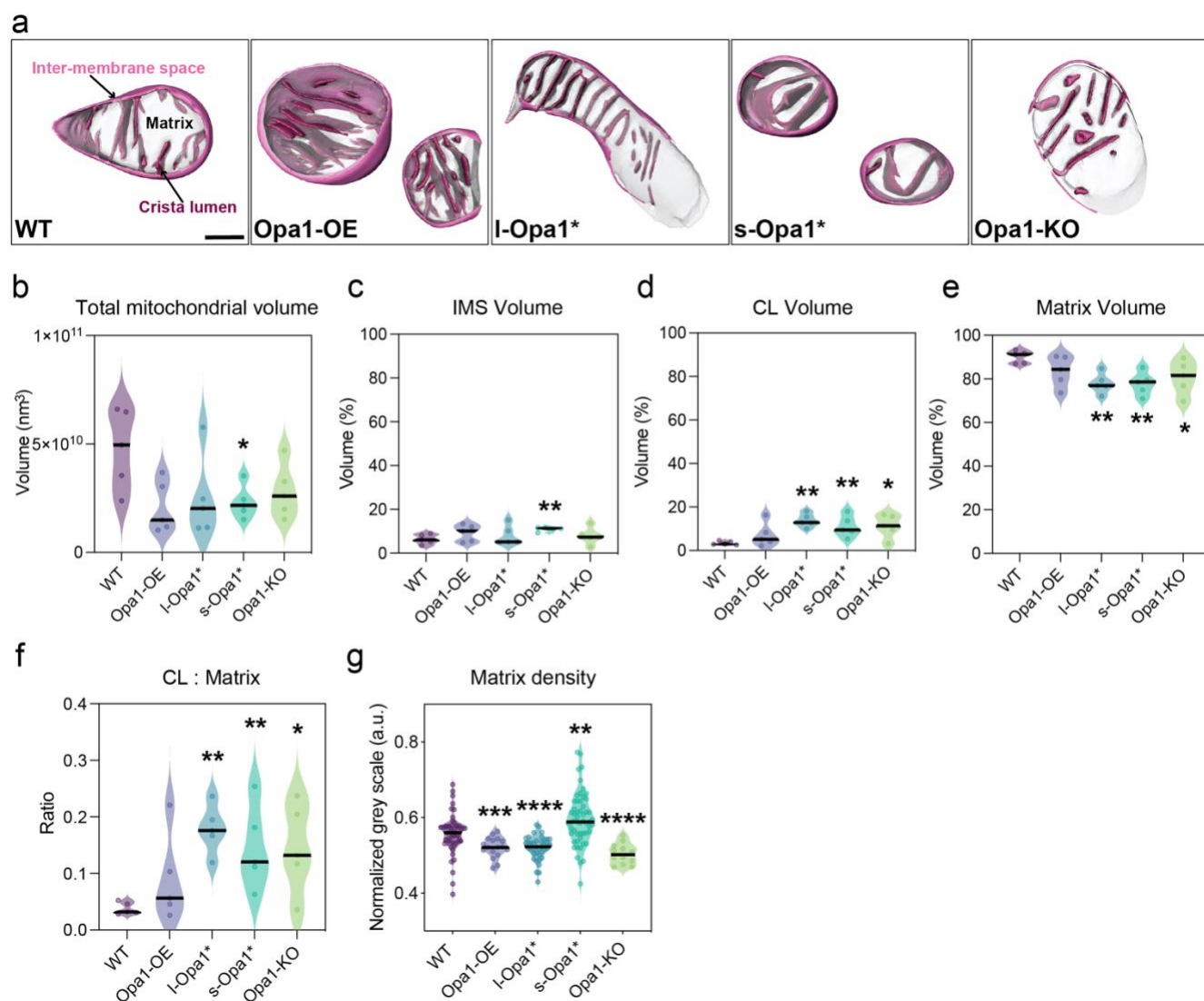


836 **Fig. 2 | *In situ* crista ultrastructure. (a)** Graph bars showing the proportions of straight, tilted, and
837 disconnected crista and **(b)** of lamellar, tubular, globular and unusual crista observed in indicated MEF
838 lines. **(c)** Measured cristae length and **(d)** cristae width across cell lines. **(e)** (Top rows) Computational
839 slices of straight, tilted, disconnected, globular and tubular crista across cell lines with zipping, pinching
840 and tight regions indicated (arrows) in 3D renderings (bottom rows) from cryo-electron tomograms. n.a.:
841 not applicable. **(f)** Histograms of crista widths across cell conditions (see Methods). **(g)** Subtomogram
842 averages of mitochondrial cristae membranes with the average width indicated. Violin graphs show data
843 distribution, the mean is shown by a bold black line. Significance of difference is tested relative to wild
844 type using Mann Whitney test; * $p < 0.05$, *** $p < 0.001$, **** $p < 0.000$. For a, b: N wild-type = 222, Opa1-OE
845 = 430, I-Opa1* = 323, s-Opa1* = 653, Opa1-KO = 243. For c, d: N = 50 for all cell lines. Scale bar = 50
846 nm.



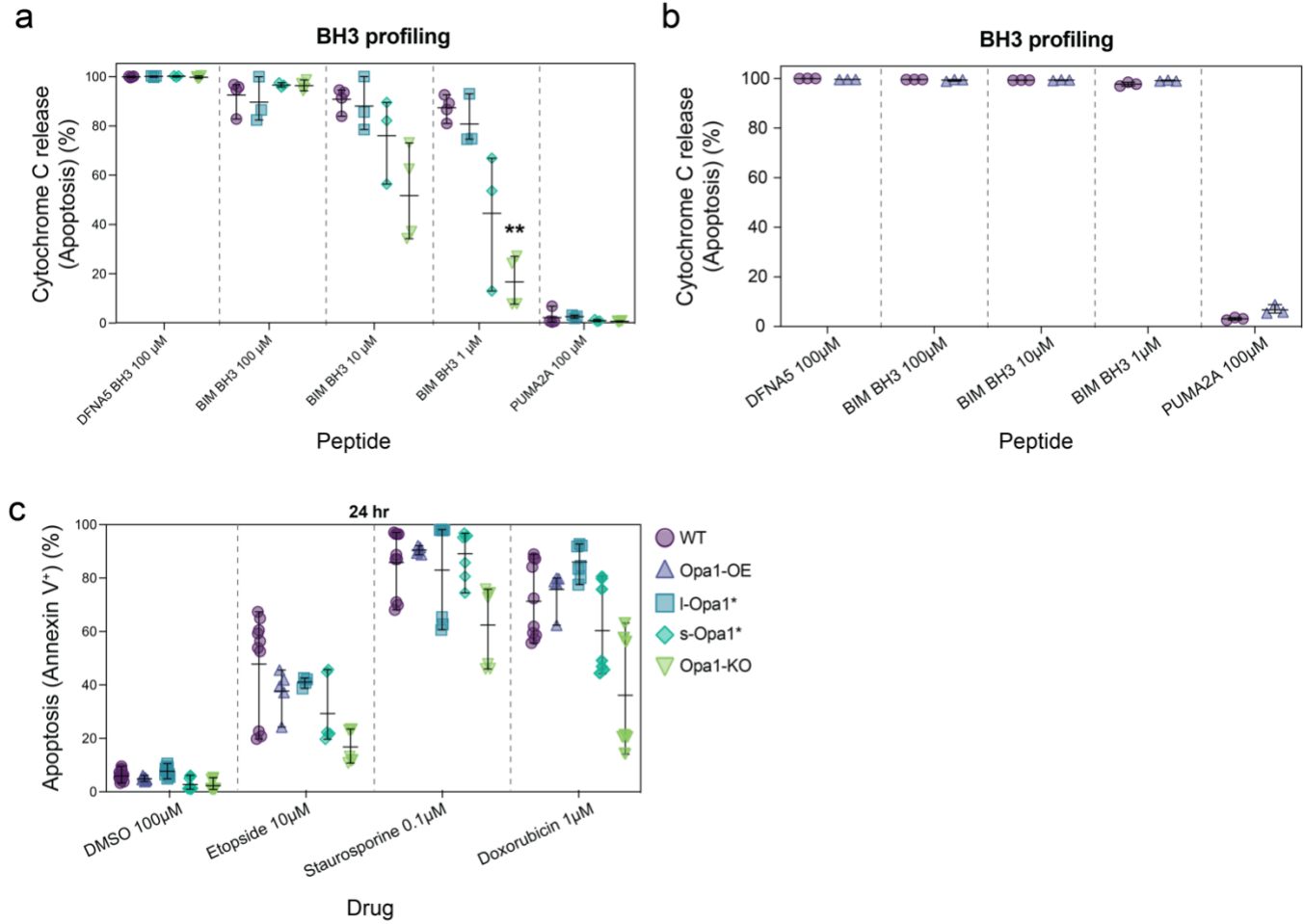
847

848 **Fig. 3 | Quantification of cristae junction (CJ) properties.** (a) Plots of measured cristae junction width
849 and (b) angle across cell lines (see Fig. S6c,d and Methods section for measurement methods). (c) (Top)
850 Summed, projected central slices of cryo-electron tomograms of representative mitochondria analyzed
851 in (a) and (b) with magnified cristae junction (bottom insets). Violin graphs show data distribution, the
852 mean is shown by a bold black line. Significance of difference is tested relative to wild type using Mann
853 Whitney test; * $p < 0.05$, ** $p < 0.005$, *** $p < 0.0005$. N: wild-type = 103, Opa1-OE = 33, l-Opa1* = 107, s-
854 Opa1* = 92, Opa1-KO = 34. Scale bar = 100 nm. Inset scale bar = 25 nm.



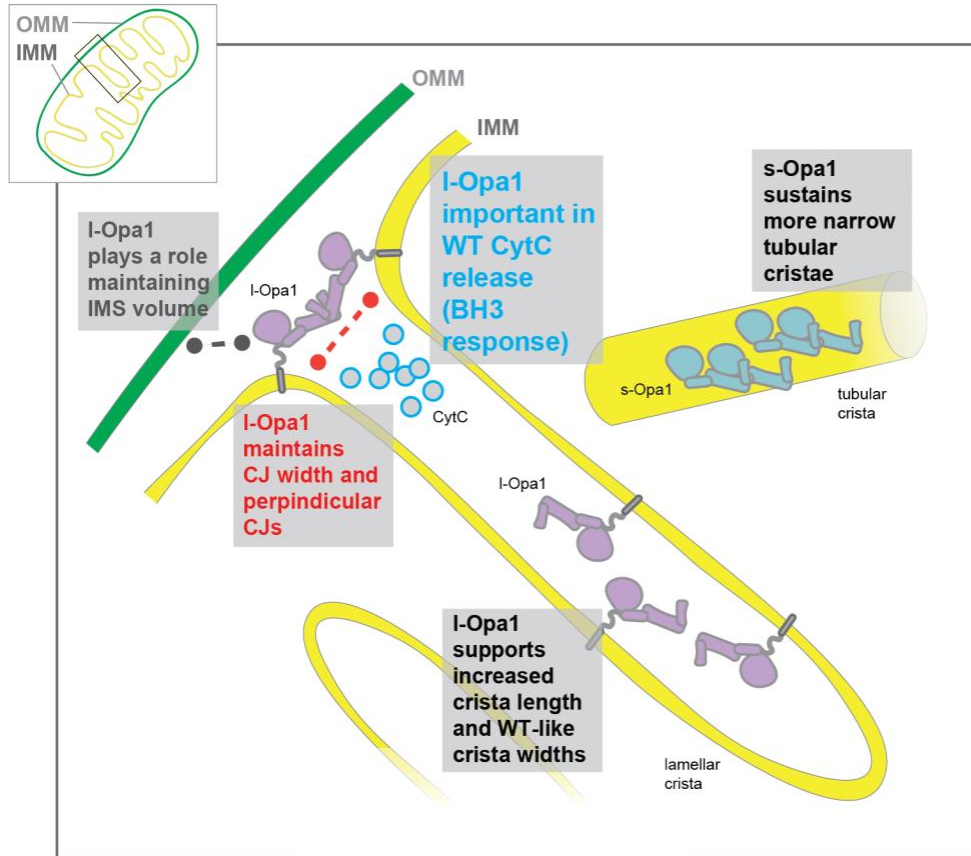
855

856 **Fig. 4 | Mitochondrial subcompartment volumes. (a)** Three-dimensional renderings of segmented
 857 inter-membrane space (IMS, pink surface), cristae lumen (CL, magenta surface), and matrix (translucent
 858 grey surface) volumes. **(b)** Total mitochondrial volume across indicated cell lines. **(c)** Quantification of
 859 IMS volume, **(d)** CL volume and **(e)** matrix volume relative to total volume of each mitochondrion indicated
 860 in (b). **(f)** CL to matrix ratio and **(g)** normalized grey scale mitochondrial matrix value across cell lines.
 861 Violin graphs show data distribution, the mean is shown by a bold black line. Significance of difference is
 862 tested relative to wild type using Mann Whitney test in b, d, e, g; *p<0.05, **p<0.01, ***p<0.001,
 863 ****p<0.0001; and unpaired t test in c: **p<0.005; N = 5 for all cell lines. Scale bar = 200 nm.



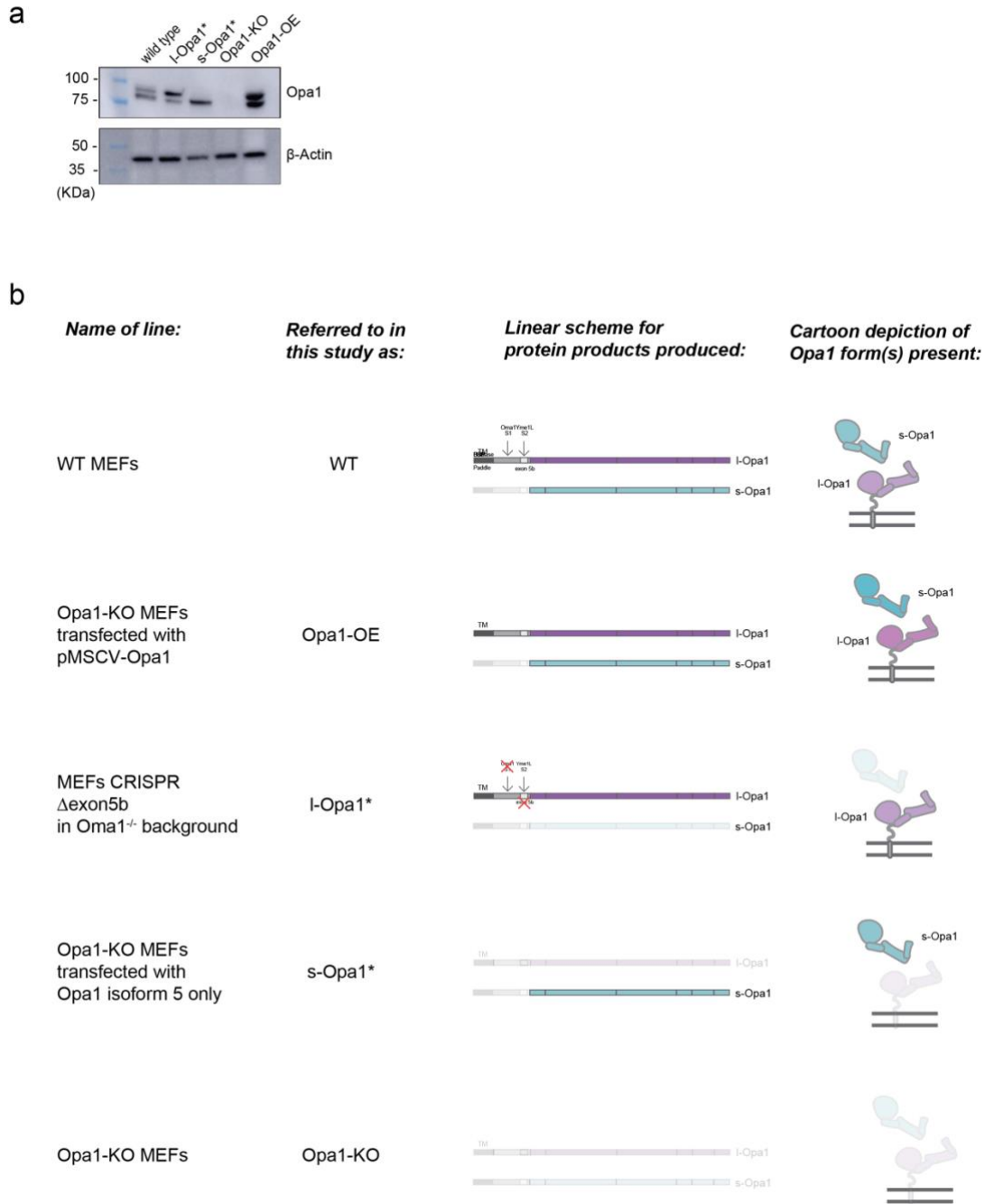
864

865 **Fig. 5 | I-Opa1* cells show WT apoptotic priming.** BH3 profiling of (a) WT, I-Opa1*, s-Opa1*, Opa1-
 866 KO and (b) WT along with Opa1-OE MEF cell lines for sensitizer BIM BH3 and PUMA. N = 3-4
 867 biological replicates. Significance of difference is tested relative to wild-type using the Holm-Sidak's
 868 multiple comparison test; **p<0.01. (c) MEF cell lines were treated with indicated agents for 24h and
 869 apoptosis was detected by Annexin V positivity staining. N = minimum 4 biological replicates.



870

871 **Fig. 6 | Summary of cryo-ET cristae observations.** Cartoon representation summarizing overarching
872 observations and hypothesis generated from this cryo-ET study. Inset: Mitochondrial cartoon IMM
873 (yellow), and OMM (green). Main panel: I-Opa1 maintains CJ width and perpendicular CJs, and
874 maintain wild-type (WT)-like cytochrome c (CytC) release properties (as evaluated by BH3 profiling). L-
875 Opa1 also plays a role in maintaining IMS volume. S-Opa1 sustains tubular and more narrow cristae.
876



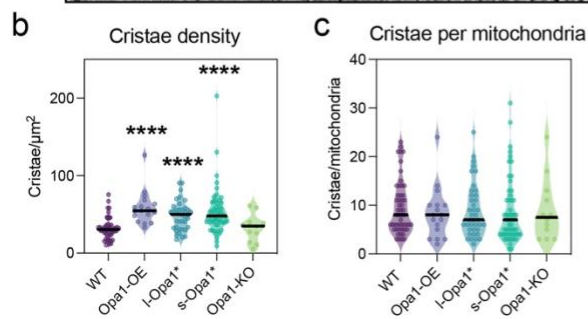
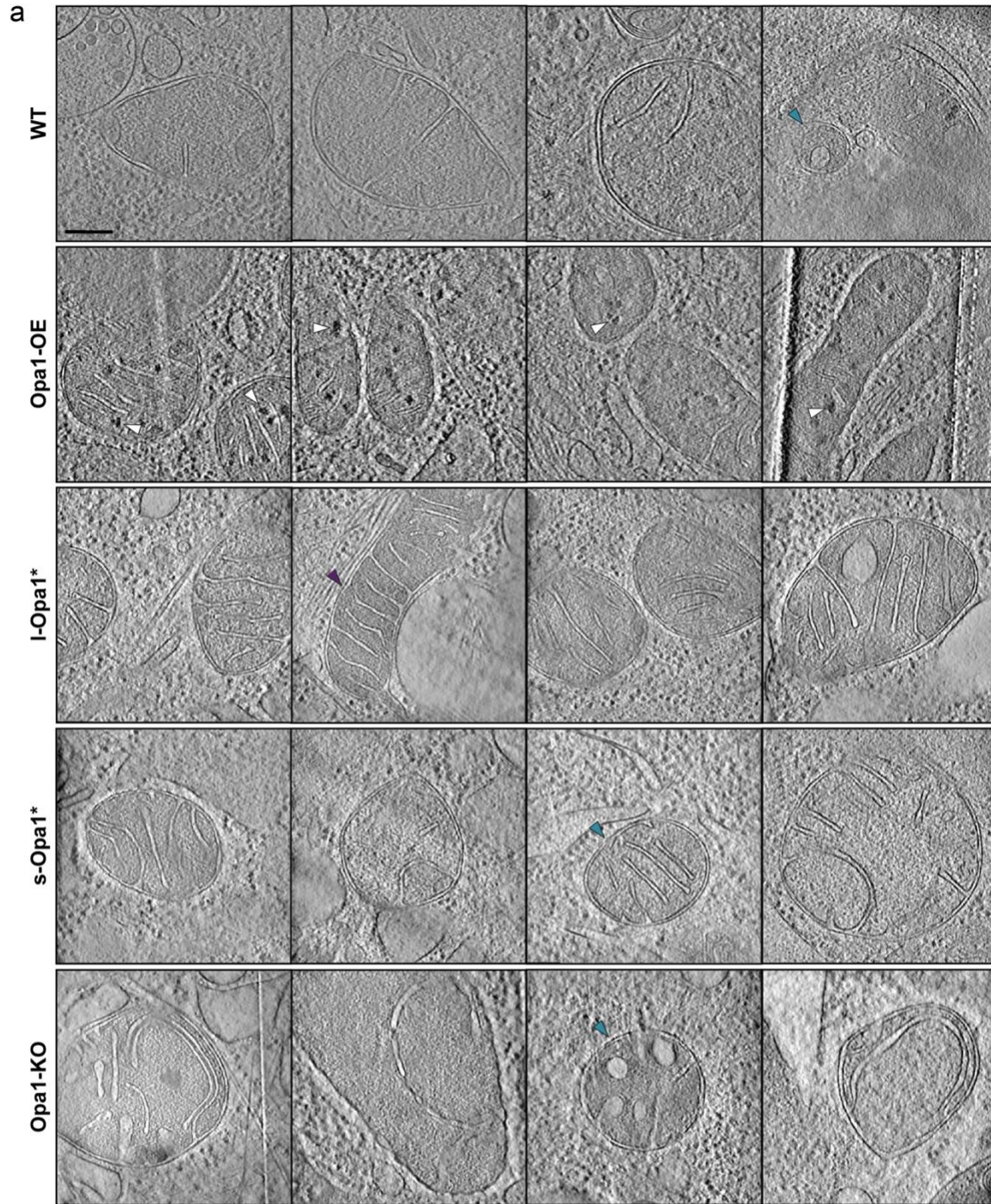
877

878

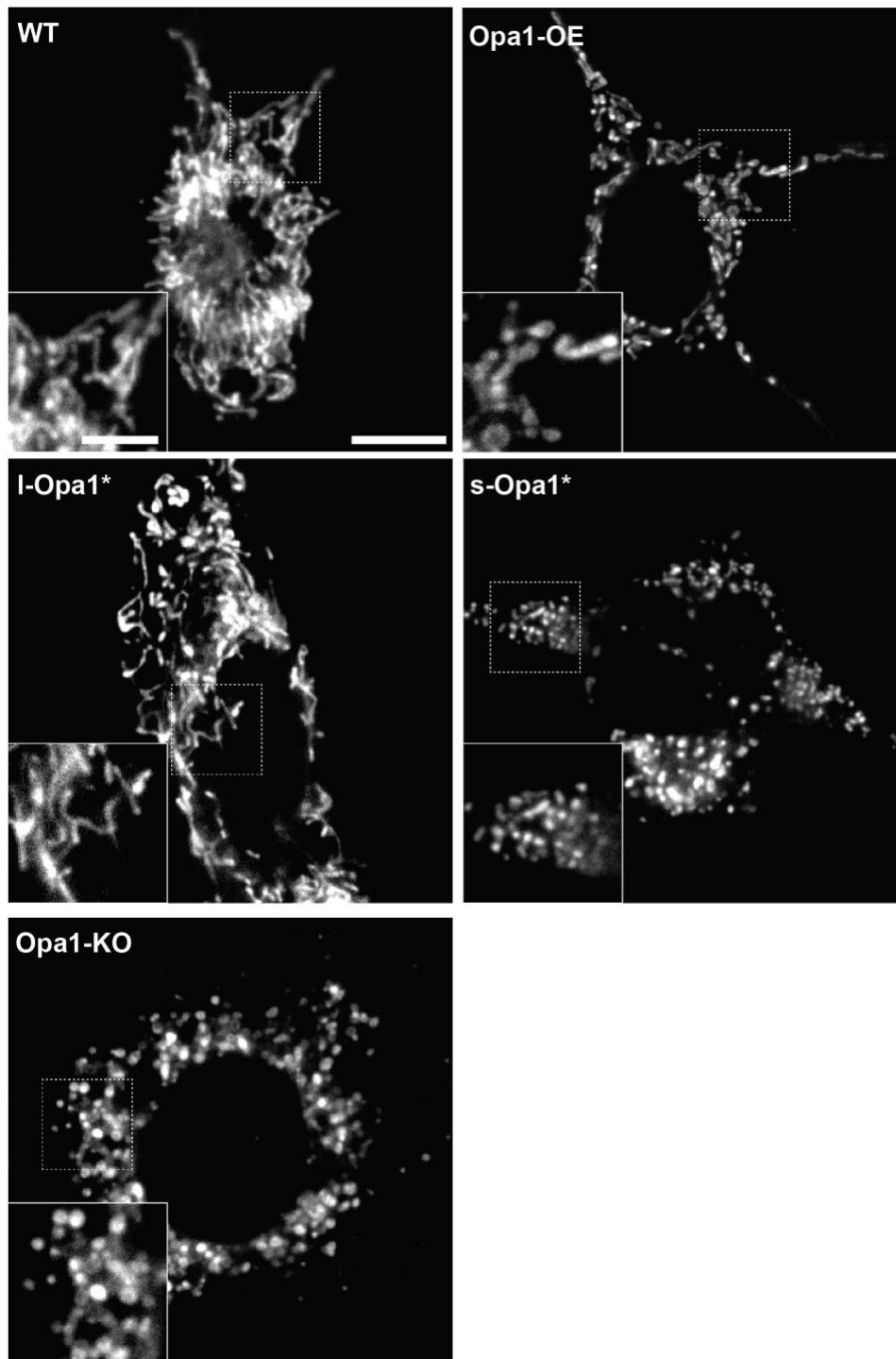
879 **Supplementary Figure S1: (a)** (Top) Western blot detection of Opa1 forms in indicated MEF cell lines

880 using Opa1 antibody. (Bottom) Actin was used as loading control. **(b)** Genetic schematic and cartoon

881 depictions of Opa1 forms present in MEF cell lines used in this study.



883 **Supplementary Figure S2: Gallery of cryo-ET data. (a)** Summed, projected central slices of cryo-
884 electron tomograms visualizing mitochondria in wild-type, Opa1-OE, l-Opa1*, s-Opa1* and Opa1-KO
885 MEFs. White arrowheads indicate calcium deposits, blue arrowheads indicate ellipsoidal mitochondria
886 and purple arrowheads indicate round mitochondria. **(b)** Plots showing mitochondrial coverage
887 (mitochondria area in μm^2 obtained from mitochondria size measurements divided by the total area of
888 the summed projected image), **(c)** mitochondria present per tomogram, **(d)** cristae density (cristae per
889 μm^2) and **(e)** cristae number per mitochondria. Violin graphs show data distribution, the mean is shown
890 by a bold black line. Significance of difference is tested relative to wild type using Mann Whitney;
891 **** $p < 0.0001$. For a: N wild-type = 51, Opa1-OE = 7, l-Opa1* = 21, s-Opa1* = 27, Opa1-KO = 11. For b:
892 N wild-type = 33, Opa1-OE = 7, l-Opa1* = 21, s-Opa1* = 28, Opa1-KO = 11. For c and d: N wild-type =
893 51, Opa1-OE = 17, l-Opa1* = 39, s-Opa1* = 55, Opa1-KO = 12. Scale bar = 200 nm.



894

895

896

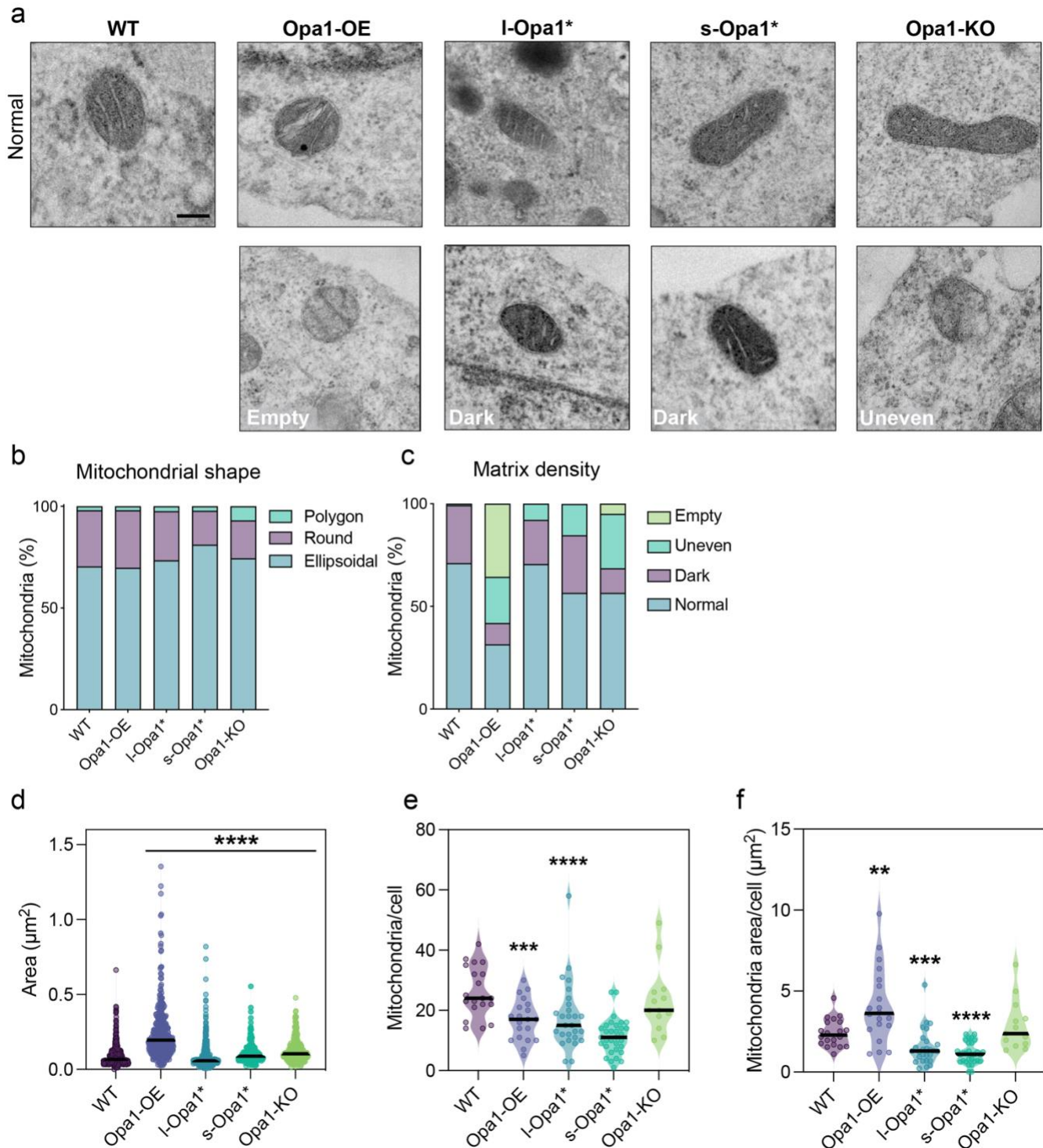
897

898

899

Supplementary Figure S3: Mitochondrial network morphology in MEF cell lines by fluorescence microscopy. Representative images of mitochondrial morphology in indicated MEF cell lines labeled with MitoTracker™ Deep Red FM. Insets show magnified view of regions indicated with dashed boxes. Scale bar = 10 μ m. Inset scale bar = 5 μ m.

900



901

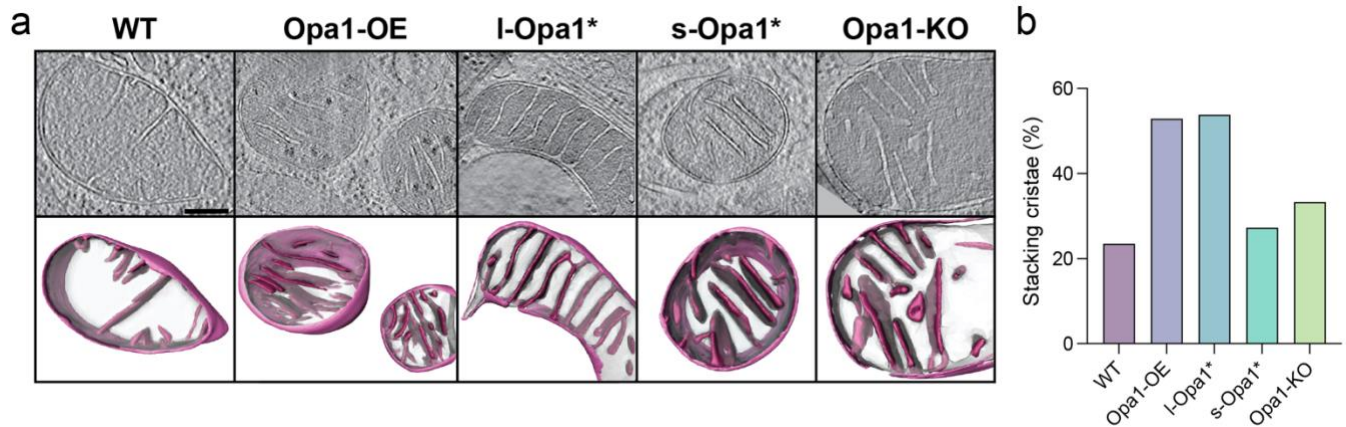
902 **Supplementary Figure S4: Mitochondrial morphology in MEF cell lines by conventional TEM. (a)**

903 Gallery of representative mitochondrial morphology observed by TEM for indicated MEF cell lines. Matrix

904 phenotype is indicated. **(b)** Graph bar representing the relative proportion of different mitochondrial

905 shapes observed. **(c)** Graph bar representing the relative proportion of mitochondrial matrix density
906 based on four categories: empty, uneven, dark and normal in indicated MEF cell lines. **(d)** Violin graphs
907 plotting mitochondrial area, **(e)** number of mitochondria per cell and **(f)** mitochondrial area in μm^2 per cell
908 in MEF cell lines included in this study. Violin graphs show data distribution, the mean is shown by a bold
909 black line. Significance of difference is tested relative to wild type using Mann Whitney; * $p < 0.05$, ** $p < 0.01$,
910 *** $p < 0.0005$, **** $p < 0.0001$. For b: N wild-type, Opa1-OE and Opa1-KO = 301, I-Opa1* = 531, s-Opa1* =
911 359. For c: N wild-type and Opa1-OE = 20, I-Opa1* = 33, s-Opa1* = 32, Opa1-KO = 13. For d: N wild-
912 type = 536, Opa1-OE = 337, I-Opa1* = 476, s-Opa1* = 318, Opa1-KO = 302. For e: N wild-type and Opa1-
913 OE = 20, I-Opa1* = 27, s-Opa1* = 32, Opa1-KO = 13. For f: N wild-type and Opa1-OE = 20, I-Opa1* =
914 27, s-Opa1* = 30, Opa1-KO = 13. Scale bar = 200 nm.
915

916

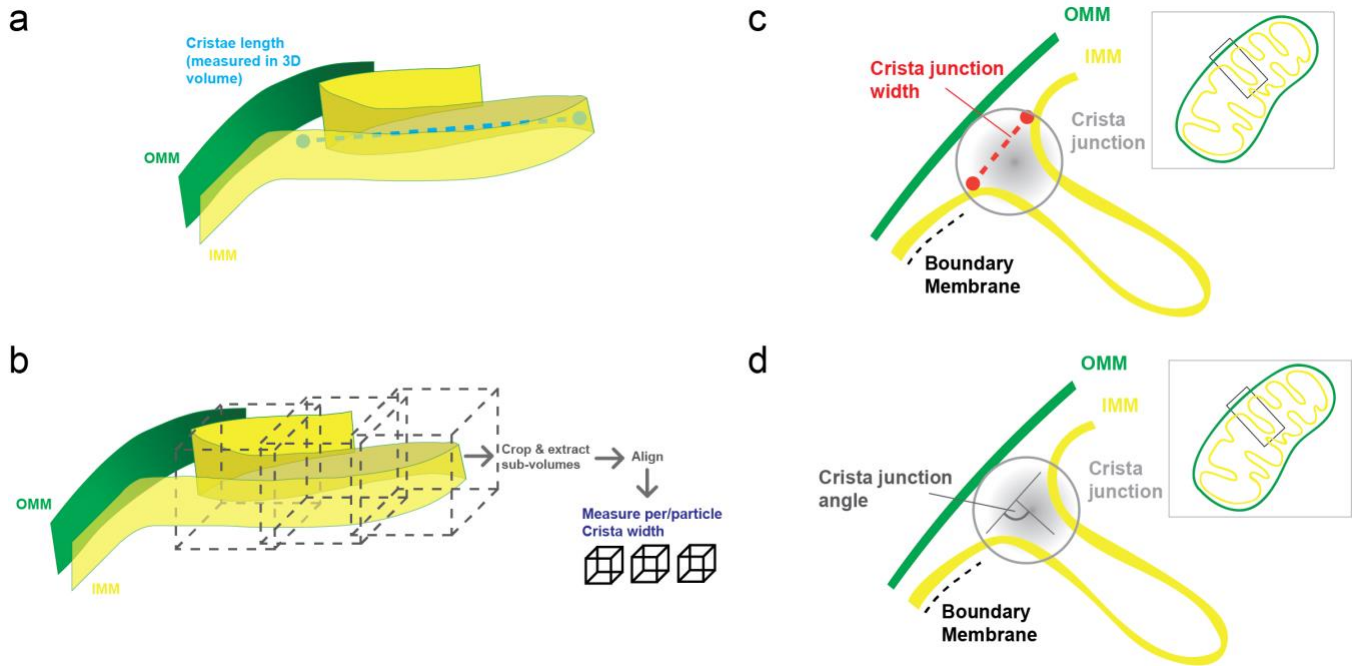


917

918 **Supplementary Figure S5: Stacking cristae.** (a) (Top) Summed, projected central slices of cryo-
919 electron tomograms visualizing mitochondria with stacking cristae characteristics, supported by 3D
920 representations consisting of their sub compartments (bottom) in indicated MEF cell lines. (b) Graph bar
921 representing percentage of mitochondria with stacking cristae formation in each MEF cell line. N: wild-
922 type = 57, Opa1-OE = 17, I-Opa1* = 39, s-Opa1* = 55, Opa1-KO = 12. Scale bar = 200 nm.

923

924



925

926

Supplementary Figure S6: Cristae length, width quantification, junction width, angle.

927

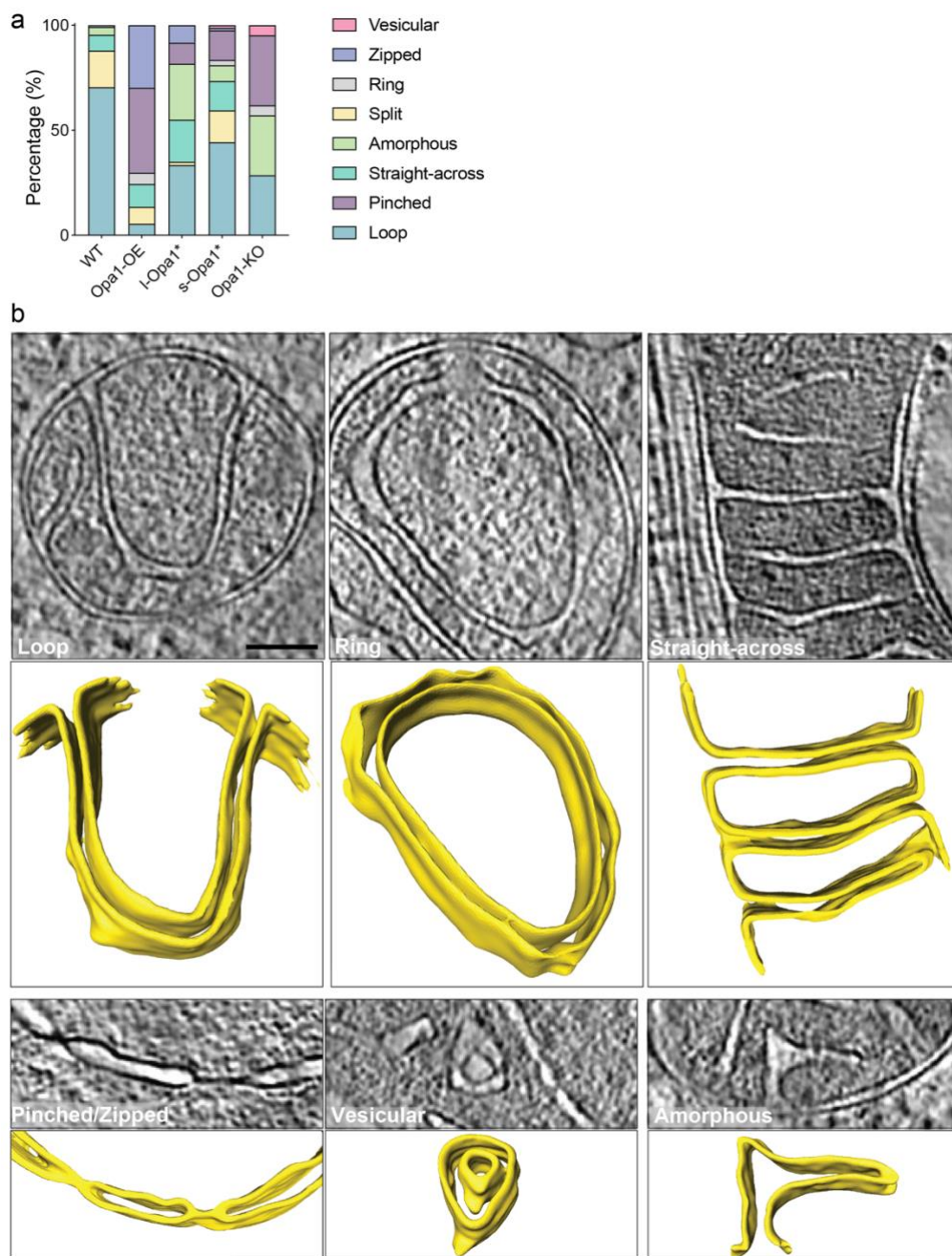
(a) Cartoon schematics representing sub-tomogram averaging (STA) approach for measuring crista

928

length and **(b)** width in 3D. **(c)** Cartoon schematic for measurement of cristae junction width and **(d)** angle.

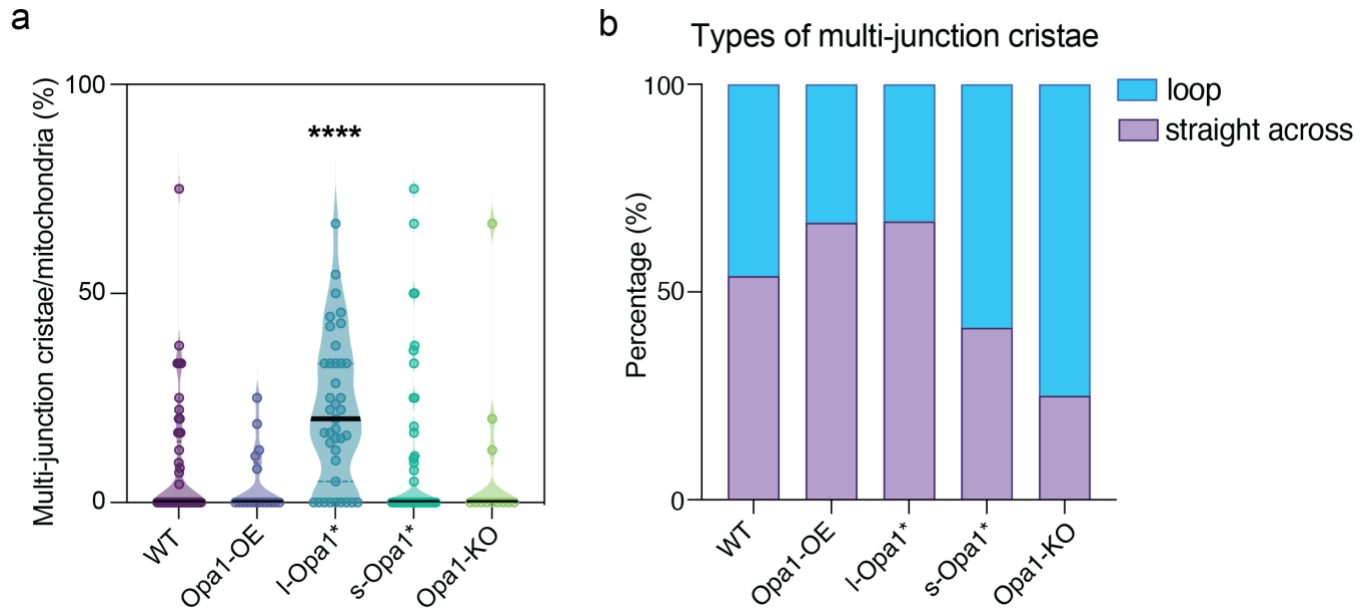
929

See Methods for details.



930

931 **Supplementary Figure S7: Unusual cristae morphology.** (a) Graph bar representing the relative
 932 proportion of unusual cristae morphology observed in indicated MEF cell lines. Unusual cristae were
 933 categorized into vesicular, zipped, ring, split, amorphous, straight-across, pinched and loop. N wild-type
 934 = 222, Opa1-OE = 430, l-Opa1* = 323, s-Opa1* = 653, Opa1-KO = 243. (b) Summed, projected central
 935 slices of cryo-electron tomograms showing examples of unusual cristae in mitochondria across cell lines
 936 in 2D (top) and 3D (bottom). Loop, ring, straight-across, pinched, vesicular, and amorphous cristae are
 937 shown. Scale bar = 200 nm.

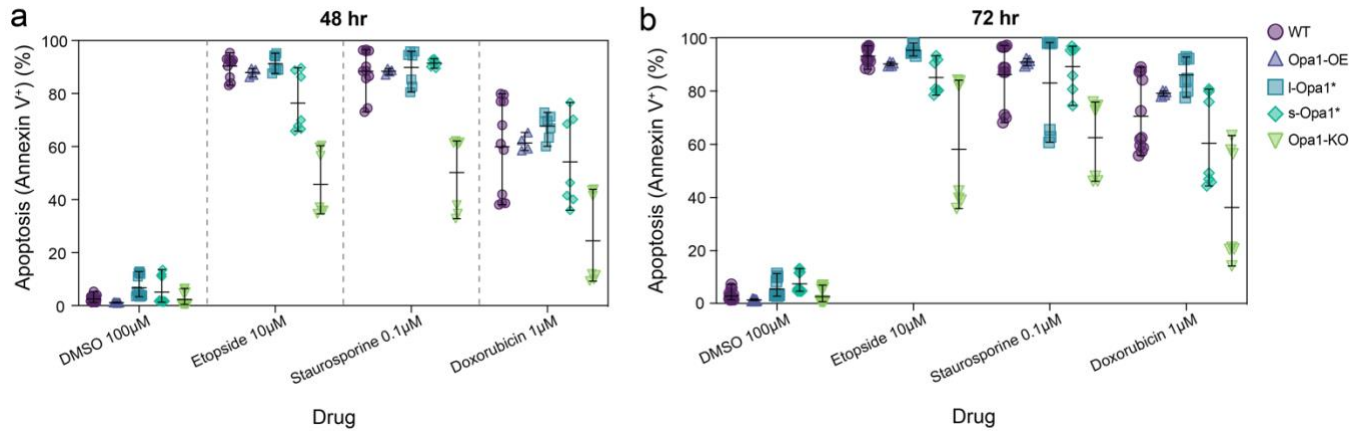


938

939 **Supplementary Figure S8: Multi-cristae junction cristae. (a)** Violin graphs plotting the percentage of
940 multi-junction cristae per mitochondrion in indicated MEF cell lines. **(b)** Graph bar representing
941 percentage of multi-junction cristae categorized into straight-across and loop morphology in each MEF
942 cell line. Violin graphs show data distribution, the mean is shown by a bold black line. Significance of
943 difference is tested relative to wild type using Mann Whitney; * $p < 0.0001$. For a: N wild-type = 18, Opa1-
944 OE = 5, I-Opa1* = 30, s-Opa1* = 16, Opa1-KO = 3. For b: N wild-type = 26, Opa1-OE = 9, I-Opa1* = 79,
945 s-Opa1* = 29, Opa1-KO = 4.

946

947



948

949

Supplementary Figure S9: Cell viability following apoptotic priming. Assessment of cell viability by Annexin V staining in MEF cell lines after treatment with the indicated compounds for **(a)** 24 hours, **(b)** 48 hours and **(c)** 72 hours. N = minimum 4 biological replicates.

951

952

953 **Movie 1:** 3D renderings of WT mitochondrial membranes (OMM in green and IMM in yellow) and
954 subcompartments (IMS in pink and CL in magenta) on tomogram Z slices in XY orientation. Scale bar =
955 200 nm.

956

957 **Movie 2:** 3D renderings of Opa1-OE mitochondrial membranes (OMM in green and IMM in yellow) and
958 subcompartments (IMS in pink and CL in magenta) on tomogram Z slices in XY orientation. Scale bar =
959 200 nm.

960

961 **Movie 3:** 3D renderings of l-Opa1* mitochondrial membranes (OMM in green and IMM in yellow) and
962 subcompartments (IMS in pink and CL in magenta) on tomogram Z slices in XY orientation. Scale bar =
963 200 nm.

964

965 **Movie 4:** 3D renderings of s-Opa1* mitochondrial membranes (OMM in green and IMM in yellow) and
966 subcompartments (IMS in pink and CL in magenta) on tomogram Z slices in XY orientation. Scale bar =
967 200 nm.

968

969 **Movie 5:** 3D renderings of Opa1-KO mitochondrial membranes (OMM in green and IMM in yellow) and
970 subcompartments (IMS in pink and CL in magenta) on tomogram Z slices in XY orientation. Scale bar =
971 200 nm.

972

973 **Movie 6:** Live-cell fluorescence microscopy of MitoTracker™ Deep Red FM-stained mitochondria in
974 indicated MEF cell lines. Movies were taken at 30 seconds per frame for 5 mins. Playback at 2 frames
975 per second (60x real-time). Scale bar = 10 μm.